Dynamics of the $O(4)$ critical point in QCD

Adrien Florio,[1,*] Eduardo Grossi,[1,2,3,†] Alexander Soloviev,[1,‡] and Derek Teaney[1,§]

[1]*Center for Nuclear Theory, Department of Physics and Astronomy,*
Stony Brook University, Stony Brook, New York 11794-3800, USA
[2]*Institut de physique théorique, Université Paris Saclay, CNRS, CEA, F-91191 Gif-sur-Yvette, France*
[3]*CPHT, CNRS, Ecole Polytechnique, IP Paris, F-91128 Palaiseau, France*

We perform a Langevin simulation of the $O(4)$ critical point, which lies in the dynamic universality class of "model G." This is the dynamic universality class of the chiral phase transition in QCD with two massless flavors. The axial charge and the order parameter $\phi_a = (\sigma, \vec{\pi})$ exhibit a rich dynamical interplay, which reflects the qualitative differences in the hydrodynamic effective theories above and below T_c. From the axial charge correlators on the critical line we extract a dynamical critical exponent of $\zeta = 1.47 \pm 0.01$(stat.), which is compatible with the theoretical expectation of $\zeta = d/2$ (with $d = 3$) when systematic errors are taken into account. At low temperatures, we quantitatively match the $O(4)$ simulations to the superfluid effective theory of soft pions.

I. INTRODUCTION

Chiral symmetry breaking and the chiral phase transition play a prominent role in QCD at finite temperature. In the limit of exactly two massless flavors $N_f = 2$, the transition from a chirally restored phase $T > T_c$, to a chirally broken phase $T < T_c$, is second order and is in the $O(4)$ universality class [1,2]. Although the static properties of the $O(4)$ critical point have been studied in detail both numerically and theoretically [3–12], the dynamic scaling properties of the critical region demand additional study, which is the goal of this work.

This study may appear academic: in the real world the finite quark mass explicitly breaks chiral symmetry, reducing the influence of the $O(4)$ critical point on the static and dynamic correlators of QCD at finite temperature. Further, the strange quark is fairly light, and the chiral transition in three-flavor QCD is first order [1]. However, lattice QCD computations of the chiral condensate as a function of quark mass show that the qualitative and, to some extent, even quantitative properties of the chiral crossover can be understood using static $O(4)$ scaling functions [13,14].

These scaling functions predict the singular behavior of the chiral condensate near the pseudocritical temperature T_{pc} and other static observables. Motivated by the lattice effort, we will perform the real-time simulations of the $O(4)$ critical region in a model system, which we hope can provide an analogous understanding of the scaling of dynamic correlators in QCD in the crossover region.

The current study is also motivated by experimental results on the momentum spectra of particles produced during the collisions of heavy ions at the Relativistic Heavy Ion Collider and the Large Hadron Collider. In much of the accessible momentum range these spectra are remarkably well described by ordinary viscous hydrodynamics [15]. From a theoretical perspective, the relevant symmetry group of QCD close to the chiral limit is approximately $SU_L(2) \times SU_R(2)$, leading to the conservation of isovector charge, and the approximate conservation of the isoaxial vector charge. The corresponding densities should be included as additional fields in the hydrodynamic description. When chiral symmetry is spontaneously broken, the pions $\vec{\pi}$ (which are the associated Goldstone bosons) should also be added to the hydrodynamic fields, and the appropriate hydrodynamics resembles a non-Abelian superfluid [16,17]. Finally, close to the $O(4)$ critical point where the σ meson is also light, the $O(4)$ order parameter $\phi_a \sim (\sigma, \vec{\pi})$ also should be included as an additional hydrodynamic degree of freedom [2,18]. Current hydrodynamic simulations do not include the isoaxial charge, the pions, or the order parameter as explicit hydrodynamic variables. By including these variables as explicit degrees of freedom we hope to increase the predictive power of hydrodynamic simulations in the crossover region.

*adrien.florio@stonybrook.edu
†eduardo.grossi@ipht.fr
‡alexander.soloviev@stonybrook.edu
§derek.teaney@stonybrook.edu

In fact, there is an excess of soft pions relative to the predictions of current ordinary hydrodynamic simulations [19–21]. We have previously suggested that this excess may reflect the cavalier treatment of chiral symmetry breaking and the $O(4)$ transition in almost all hydrodynamic simulations of heavy-ion collisions to date [18]. To corroborate this suggestion, we will need to simulate the real-time dynamics of the $O(4)$ phase transition for an expanding fluid. As discussed in [18], the dynamics of the order parameter matches smoothly onto a pion-hydro effective-field theory (EFT) for $T \lesssim T_c$; this pion EFT subsequently matches onto a kinetic description for soft pion particles coupled to the background fluid flow [17]; and finally, the kinetics can be used to propagate pions to freeze-out with definite predictions for soft pions yields and their correlations. In addition there is an experimental proposal to measure soft pions and their correlations over a wide range in rapidity [22], which is ideally suited to unravel this physics and to probe the (in)applicability of ordinary hydrodynamics in this regime.

As a first step, we will compute the real-time correlation functions of a model $O(4)$ critical system with Langevin simulations and study their scaling properties. There is considerable theoretical interest in the critical correlators themselves. Many years ago Rajagopal and Wilczek determined that the dynamic universality class of QCD is similar to "model G" of [23], where the order parameter $\phi_a = (\sigma, \vec{\pi})$ is not conserved, but has a nontrivial Poisson bracket with vector and axial vector charges [2]. They also determined dynamical critical exponent to be $\zeta = \frac{d}{2}$, which we find in the simulations presented here. Because the critical theory must transition between ordinary hydro at high temperatures and a non-Abelian superfluid hydro at low temperatures, the expected structure of the hydrodynamic correlations functions is rich [18]. It would be nice to see this structure in a simulation.

Earlier numerical studies on the critical dynamics of field theories [including $O(4)$ symmetric ones] have been performed in the "classical-statistical" framework [24–26]. Given some relativistic quantum-field theory, the high-temperature spectral functions are saturated by their classical counterparts close to the critical point. Since the nonanomalous symmetries and conservation laws of the classical-field theory are shared with the quantum one, the classical dynamics belongs to the same dynamic universality class as the full quantum theory. Of particular relevance to our work was the study done in [25], which studied a classical relativistic $O(4)$ model, and determined the spectral functions of the order parameter. The spectral functions were shown to display the appropriate behavior as a function of temperature, and pion quasiparticle poles were observed in the broken phase. Because the classical model has $O(4)$ Noether charge densities, $n_{ab} \sim \phi_{[a}\partial_t \phi_{b]}$, which have a nontrivial Poisson bracket with the order parameter, the dynamics of this model should lie in the

universality class of model G. However, within this setup studying the model G dynamics is difficult, since rapidly oscillating UV modes (which build up the charge densities microscopically) must be carefully evolved. Consequently, a conclusive extraction of the dynamical critical exponent was not possible, and the interplay between the order parameter and the axial charge was not studied. Very recently [27], the same group adopted an approach for "model B" and "model D," which is somewhat closer in spirit to the one taken here for model G, where the charge densities are treated as additional slow variables. In their recent work, Israel-Stewart-like diffusion models belonging to the specified dynamical class (B or D) were simulated, and a careful study of the dynamical scaling function and of their momentum dependence was performed. In particular, this work constitutes an important stepping stone towards the study of "model H," which is believed to describe the universality class of the speculated QCD critical point [28].

An outline of the paper is as follows. In Sec. II we discuss the model equations we will solve. Of particular interest is the numerical strategy presented in Sec. II C, which may be useful for other model systems. In Sec. III A we will review the thermodynamics of the model and fix the nonuniversal (thermodynamic) parameters of the model. Finally in Sec. IV we turn to the dynamical properties of the model presenting the principal results. In Sec. IV B we present a qualitative overview of the phase transition, and examine the dynamics in the chirally restored limit. Then in Sec. IV C, we examine the low-temperature limit where the $O(4)$ dynamics should match with the pion EFT. We examine the Gell-Mann-Oakes-Renner relation, and the dissipative pion dynamics proposed by Son and Stephanov [29,30]. In the last section, Sec. IV D, we examine the scaling of correlation functions along the critical line. We extract the dynamical critical exponent ζ and find $\zeta \simeq 1.47 \pm 0.01(\text{stat.})$, which is very close to the predictions of Rajagopal and Wilczek of $\zeta = d/2$. Finally, a short outlook is presented in Sec. V.

II. MODEL

A. Model equations

QCD with two degenerate massless quarks is well known to have a second-order phase transition and is in the universality class of the $O(4)$ critical point. Dynamical properties of a theory near a continuous phase transition are also universal, but theories with the same static properties can lead to different dynamical universality classes. Different dynamics arise because of the existence or nonexistence of conserved charges in the theory [23]. As pioneered in [2] (see [18] for a recent review) the dynamics of the QCD $O(4)$ critical point is the one of an $O(4)$ antiferromagnet, model G of [23].

Model G consists of an $O(4)$ order parameter[1] $\phi_a = (\sigma, \vec{\pi})$ field, and adjoint charge densities n_{ab}. The field ϕ is a proxy for the quark condensate $\langle \bar{q}_R q_L \rangle$, and as a result is not a conserved quantity. The antisymmetric tensor of charge densities n_{ab} can be decomposed into a vector part, $n_V^s = \frac{1}{2}\epsilon^{s s_1 s_2} n_{s_1 s_2}$, and an axial part, $n_A^s = n_{0s}$. They represent the original isovector $\vec{n}_V \sim \bar{q}\gamma^0 \vec{t}_I q$ and isoaxial $\vec{n}_A \sim \bar{q}\gamma^0 \gamma^5 \vec{t}_I q$ charge densities. The vector current is exactly conserved for equal quark masses, while the axial current is only approximately conserved, since the finite quark mass explicitly breaks the chiral $SU_L(2) \times SU_R(2) \sim O(4)$ symmetry. The explicit symmetry breaking is taken into account by adding an external magnetic field $H_a = (H, \vec{0})$ to the effective action. The equilibrium action (or effective Hamiltonian) thus takes a Landau-Ginzburg form:

$$\mathcal{H} \equiv \int d^3x \left[\frac{n^2}{4\chi_0} + \frac{1}{2}\partial_i\phi_a \partial^i\phi_a + V(\phi) - H \cdot \phi \right]. \quad (1)$$

Here $n^2 = n_{ab}n_{ab}$ and

$$V(\phi) = \frac{1}{2}m_0^2 \phi^2 + \frac{\lambda}{4}(\phi \cdot \phi)^2, \quad (2)$$

with m_0^2 negative. As reviewed below, the relevant hydrodynamic equations of motion for these fields are [2]

$$\partial_t\phi_a + g_0\mu_{ab}\phi_b = -\Gamma_0 \frac{\delta\mathcal{H}}{\delta\phi_a} + \theta_a, \quad (3a)$$

$$= \Gamma_0\nabla^2\phi_a - \Gamma_0(m_0^2 + \lambda\phi^2)\phi_a + \Gamma_0 H_a + \theta_a, \quad (3b)$$

$$\partial_t n_{ab} + g_0\nabla\cdot(\nabla\phi_{[a}\phi_{b]}) + H_{[a}\phi_{b]} = \sigma_0\nabla^2\frac{\delta\mathcal{H}}{\delta n_{ab}} + \partial_i\Xi^i_{ab}, \quad (3c)$$

$$= D_0\nabla^2 n_{ab} + \partial_i\Xi^i_{ab}. \quad (3d)$$

Here, for example, $H_{[a}\phi_{b]}$ denotes the antisymmetrization, $H_a\phi_b - H_b\phi_a$. χ_0 is the isovector and the isoaxialvector charge susceptibility; these susceptibilities are equal and approximately constant near the critical point. μ_{ab} is the chemical potential, n_{ab}/χ_0. The coefficients Γ_0 and σ_0 are the bare kinetic coefficients associated with the order parameter and the charges. The bare diffusion coefficient of the charges is $D_0 = \sigma_0/\chi_0$. The constant g_0 is a coupling of the field ϕ, and has the units of (action)$^{-1}$ in our conventions. Finally, θ_a and Ξ_{ab} are the appropriate noises, which are defined through their two-point correlations [23]:

$$\langle \theta_a(t,x)\theta_b(t',x')\rangle = 2T_c\Gamma_0\delta_{ab}\delta(t-t')\delta^3(x-x'), \quad (4a)$$

$$\langle \Xi^i_{ab}(t,x)\Xi^j_{cd}(t',x')\rangle = 2T_c\sigma_0\delta^{ij}(\delta_{ac}\delta_{bd} - \delta_{ad}\delta_{bc})\delta(t-t') \\ \times \delta^3(x-x'). \quad (4b)$$

Let us briefly review the equations of motion, referring to the literature for the general strategy [23,31] and the specifics of the $O(4)$ model [2,18]. Since the correlation lengths are long compared to all microscopic lengths,

hydrodynamics is the appropriate framework to describe the evolution of the order parameter and conserved quantities near the critical point. The hydrodynamic equations written in (3) naturally break up into an ideal evolution (the left-hand side of the equations) with viscous damping (the right-hand side of the equations). Quite generally, the ideal hydrodynamics follows from the Poisson brackets and conservation laws of the system, which are dictated by symmetry [31]. For instance, the conserved charges $Q_{ab} = \int_x n_{ab}(x)$ generate $O(4)$ rotations. If this property is shared by the corresponding classical dynamics, the Poisson bracket between the charge density and the order parameter takes a prescribed form:

$$\{n_{ab}(x), \phi_c(y)\} = g_0(\mathcal{J}_{ab})_{cd}\phi_d(y)\delta^{(3)}(x-y), \quad (5)$$

where g_0 is a unit of $1/(\text{action})$, and $(\mathcal{J}_{ab})_{cd} = \delta_{ac}\delta_{bd} - \delta_{ad}\delta_{ab}$ are the matrices of the $O(4)$ Lie algebra.[2] Indeed, given the Poisson bracket in (5), the ideal part of the evolution in (3) takes the form

---

[1]Here a and b denote $O(4)$ indices; s, s_1, s_2, etc. denote the isospin indices, i.e., the components of $\vec{\pi}$; finally, spatial indices are notated i, j and k. The dot product indicates an appropriate contraction of indices when clear from context, e.g., $\phi \cdot \phi = \phi_a\phi_a$, $\vec{\pi}\cdot\vec{\pi} = \pi_s\pi_s$, and $\nabla\cdot\nabla = \partial_i\partial^i$.

[2]More explicitly, the 4×4 infinitesimal $O(4)$ rotations are parametrized by $R \simeq 1 + \frac{1}{2}\delta\theta\cdot\mathcal{J}$. The infinitesimal rotation generated by Q is $\phi \rightarrow \phi + \frac{1}{2g_0}\{\delta\theta\cdot Q, \phi\}$ leading ultimately to Eq. (5).

$$\partial_t \phi_a + \{\mathcal{H}, \phi_a\} = 0, \tag{6a}$$

$$\partial_t n_{ab} + \{\mathcal{H}, n_{ab}\} = 0. \tag{6b}$$

It is also easy to verify directly from (3) that the ideal evolution leaves $\mathcal{H} = $ const. The structure of the dissipative fluxes and corresponding noises are found by expanding the dissipative flux in terms of the corresponding conjugate variables and demanding the entropy production be positive [18,32]. This leads to a simple relaxation equation for the nonconserved order parameter and a diffusion equation for the (partial) currents.

$$\partial_t \phi_a + \{H, \phi_a\} = -\Gamma_0 \frac{\delta \mathcal{H}}{\delta \phi_a} + \theta_a, \tag{7}$$

$$\partial_t n_{ab} + \{H, n_{ab}\} = \sigma_0 \nabla^2 \frac{\delta \mathcal{H}}{\delta n_{ab}} + \partial_i \Xi_{ab}^i. \tag{8}$$

A standard set of steps shows that Fokker-Plank evolution associated with the complete stochastic process of this form asymptotes to the required equilibrium probability distribution [33]:

$$P(\phi, n) = Z e^{-H[\phi, n]/T_c}. \tag{9}$$

The thermodynamics of this model is recalled in [18] and we will determine some static properties of relevance in Sec. III A. The real-time correlation functions we will study here are

$$G_{\sigma\sigma}(t, k) \equiv \frac{1}{V} \langle \sigma(t, \mathbf{k}) \sigma(0, -\mathbf{k}) \rangle_c, \tag{10a}$$

$$G_{\pi\pi}(t, k) \equiv \frac{1}{3V} \sum_s \langle \pi_s(t, \mathbf{k}) \pi_s(0, -\mathbf{k}) \rangle_c, \tag{10b}$$

$$G_{AA}(t, k) \equiv \frac{1}{3V} \sum_s \langle n_A^s(t, \mathbf{k}) n_A^s(0, -\mathbf{k}) \rangle_c, \tag{10c}$$

where $\langle \ldots \rangle_c$ refers to a connected two-point function. We will limit this study to $k = 0$.

Close to the critical point, the dynamics is expected to be controlled by "dynamic scaling" [23]. In particular, we expect the time development of our two-point functions to scale with the correlation length ξ as

$$G_{\sigma\sigma}(t, k) = \chi_{\parallel}(k) Y_\sigma(\Omega \xi^{-\zeta} t, \xi k, z), \tag{11a}$$

$$G_{\pi\pi}(t, k) = \chi_{\perp}(k) Y_\pi(\Omega \xi^{-\zeta} t, \xi k, z), \tag{11b}$$

$$G_{AA}(t, k) = \chi_0 Y_A(\Omega \xi^{-\zeta} t, \xi k, z). \tag{11c}$$

Here the functions $\chi_{\parallel}(k)$, $\chi_{\perp}(k)$ are the static order parameter susceptibilities, and depend on k and ξ; χ_0 is

corresponding charge susceptibility which lacks these dependencies; Ω is a nonuniversal constant normalizing the time; finally, z is the familiar static scaling variable involving the reduced temperature and magnetic field (see below). Y_σ, Y_π, and Y_A are universal dynamical scaling functions and ζ is the corresponding dynamical critical exponent of the theory. The expected dynamical critical exponent for model G is $\zeta = d/2$ [2]. The scaling form (with $\zeta = d/2$) implies that if the correlation length increases by a factor of 2, then the characteristic relaxation time increases by a factor of $2^{3/2}$, thereby exhibiting a "critical slowing down."

B. Lattice units and matching the model to QCD

To simulate the model, we begin by taking g_0 and T_c as our microscopic units of $(\text{action})^{-1}$ and energy, respectively, setting $g_0 = T_c = 1$ in the computer code. Similarly, we will choose a microscopic length a as the cutoff in our problem, setting the lattice spacing to unity in the code.

As a result of these choices, the quantities we measure directly from our simulations are expressed in lattice units, and they are dimensionless numbers. To convert these quantities to physical predictions, we need to assign a physical value to g_0, T_c, and a. The critical temperature T_c can be matched directly to the QCD critical temperature. Once T_c is fixed, $g_0 T_c$ is adjusted so that the model reproduces the pole frequency of the pion. Lastly, the cutoff a can be adjusted so that our system reproduces the correlation length of QCD. The aim of this section is to explain this procedure in greater detail. Before doing so, let us note that our set of units, $g_0 = T_c = a = 1$, will be implicit both in the figures and the text. However in this section, and if necessary for clarity, we will adopt a "hat" notation for variables in lattice units, e.g., $\hat{n} = na^3$ and $\hat{\chi} = T_c \chi a^3$ are the dimensionless charge density and charge susceptibility, respectively.

The model has an $O(4)$ critical point at a critical mass parameter $\hat{m}_c^2(\lambda)$. At infinite volume and close to the critical point, the dependence of the model condensate (in units of $\sqrt{T_c/a}$) on the mass parameter and magnetic field takes the conventional scaling form [6]

$$\hat{\bar{\sigma}} = h^{1/\delta} f_G(z), \tag{12}$$

where δ is the critical exponent, and $f_G(z)$ is a universal function with $f_G(0) = 1$. Here h is the reduced magnetic field and z is the scaling variable,

$$h \equiv \frac{\hat{H}}{\hat{H}_0}, \qquad z \equiv \bar{t}_r h^{-1/\beta\delta}, \quad \text{with} \quad \bar{t}_r \equiv \frac{\hat{m}_0^2 - \hat{m}_c^2}{\mathfrak{m}^2}, \tag{13}$$

while $\hat{m}_c^2(\lambda)$, $\hat{H}_0(\lambda)$, and $\mathfrak{m}^2(\lambda)$ are order-1 nonuniversal constants that are fit to our numerical data on thermodynamics [see Sec. III A and Eq. (30)]. In physical units,

$$\hat{\bar{\sigma}} = \frac{\sigma}{B^{O(4)}}, \quad \text{with} \quad B^{O(4)} = \sqrt{\frac{T_c}{a}}. \quad (14)$$

In QCD, the chiral condensate close to the critical point takes the same form $\langle \bar{q}q \rangle / B^{\mathrm{QCD}} = h^{1/\delta} f_G(z)$, but with scaling variables

$$z \equiv \left(\frac{T - T_c}{T_c} \right) h^{-1/\beta\delta}, \qquad h \equiv \frac{m_q c^2}{H_0^{\mathrm{QCD}}}. \quad (15)$$

Evidently, to match the two systems we are to equate the scaling variables, h and z, and equate the order parameters:

$$\frac{\langle \bar{q}q \rangle}{B^{\mathrm{QCD}}} = \hat{\bar{\sigma}} = \frac{\bar{\sigma}}{B^{O(4)}}. \quad (16)$$

For H small and $T < T_c$, the universal function $f_G(z)$ behaves as z^β, and the model condensate takes the form

$$\hat{\bar{\sigma}} = \left(\frac{\hat{m}_c^2 - \hat{m}_0^2}{\mathfrak{m}^2} \right)^\beta, \quad (17)$$

while chiral condensate takes an analogous form at the corresponding z:

$$\frac{\langle \bar{q}q \rangle}{B^{\mathrm{QCD}}} = \left(\frac{T - T_c}{T_c} \right)^\beta, \quad (18)$$

providing an explicit map between $(T - T_c)/T_c$ and the mass parameter of the model.

The constant B^{QCD} has units of $(\text{meters})^{-3}$ and H^{QCD} has unit of energy. They can be chosen arbitrarily, but not independently, as the parameter

$$\xi_1^{\mathrm{QCD}} = \left(\frac{H_0^{\mathrm{QCD}} B_0^{\mathrm{QCD}}}{T_c} \right)^{-1/d}, \quad (19)$$

fixes a microscopic unit of length. The diverging correlation length of QCD near the critical point is a universal function times this length [34]. As we show in Appendix A 1, by choosing

$$a = \hat{H}_0^{1/d} \xi_1^{\mathrm{QCD}}, \quad (20a)$$

$$g_0 = \frac{1}{\hbar}, \quad (20b)$$

the model will reproduce both the correlation length and pole frequency of the pion in QCD.

Having set three of our parameters to unity to fix our units of space, time, and energy, we are still left with three more dimensionless parameters which must be specified, namely

$$\hat{\chi}_0 \equiv T_c \chi_0 a^3, \quad \hat{\Gamma}_0 \equiv \Gamma_0 \left(\frac{1}{g_0 T_c a^2} \right), \quad \text{and} \quad D_0/\Gamma_0. \quad (21)$$

The susceptibility χ_0 sets the magnitude of charge fluctuations relative to the fluctuations of the order parameter, while Γ_0 and D_0 determine the relaxation of the order parameter and the charge diffusion, respectively.

Switching to the conventional $\hbar = c = 1$ units for this paragraph, for the system under study there really is only one scale $T_c \sim \Lambda_{\mathrm{QCD}}$. We expect that the microscopic (i.e., cutoff) length and time are both of order $\sim 1/T_c$. The susceptibility in units of T_c is also of order unity. Indeed, we expect that all dimensionless constants are of order unity, and therefore, in this study we will take

$$\hat{\chi}_0 = 5, \qquad \hat{\Gamma}_0 = 1, \quad \text{and} \quad D_0/\Gamma_0 = \frac{1}{3}, \quad (22)$$

for definiteness. It may be worthwhile to explore the dependencies on these parameters further, but we have not done so here.

C. Numerical strategy

To simulate the real-time dynamics, we will discretize the stochastic evolution equations in (3a) and (3b), placing the system on a spatial lattice of size L and volume $V = L^3$. We briefly present our algorithm in this section; the interested reader can find detailed explanations in Appendix A.

As the equations naturally separate into an ideal and a dissipative part, we use an "operator splitting" approach. In spirit, we first evolve our fields for a short time, neglecting the dissipative part:

$$\partial_t \phi_a \approx -\mu_{ab} \phi_b, \quad (23a)$$

$$\partial_t n_{ab} \approx -\partial_i (\partial^i \phi_{[a} \phi_{b]}) - H_{[a} \phi_{b]}, \quad (23b)$$

where spatial derivatives are discretized appropriately. We then neglect the ideal part and solve for the dissipative dynamics:

$$\partial_t \phi_a \approx -\Gamma_0 \frac{\delta \mathcal{H}}{\delta \phi_a} + \theta_a, \quad (24a)$$

$$\partial_t n_{ab} \approx \sigma_0 \nabla^2 \frac{\delta \mathcal{H}}{\delta n_{ab}} + \partial_i \Xi_{ab}^i. \quad (24b)$$

Decoupling the equations in such a way allows us to use methods specifically tailored to the two different dynamics. In particular, we use a symplectic integrator to evolve the ideal part, preserving in this way the underlying Poisson bracket structure. To simulate the dissipative Langevin dynamics, we use a Metropolis algorithm. A similar strategy to simulate the Langevin dynamics was used

previously to calculate the sphaleron transition rate in hot non-Abelian plasmas[3] [35]. At every lattice site x, the order parameter is updated as

$$\phi_a(t + \Delta t, x) = \phi_a(t, x) + \Delta\phi_a, \qquad (25)$$

where for each flavor index a the increment is

$$\Delta\phi_a = \sqrt{2\Delta t \Gamma_0}\, \xi_0.$$

Here ξ_0 is a random number with unit variance $\langle \xi_0^2 \rangle = 1$. The update proposal is accepted with probability $\min(1, e^{-\Delta H})$, where ΔH is the change in the discretized Hamiltonian. If the proposal is rejected, then $\phi(t + \Delta t, x) = \phi(t, x)$. For small $\Delta\phi_a$

$$\Delta H \approx \left.\frac{\delta\mathcal{H}}{\delta\phi_a}\right|_{\phi_a(x,t)} \Delta\phi_a, \qquad (26)$$

which can be used to show straightforwardly that the mean and variance of the accepted proposals reproduce the dissipative and stochastic terms of the Langevin process (see also Appendix A for more details):

$$\overline{\phi_a(t + \Delta t, x) - \phi_a(t, x)} \approx -\Delta t \Gamma_0 \frac{\delta\mathcal{H}}{\delta\phi_a}, \qquad (27a)$$

$$\overline{(\phi_a(t + \Delta t, x) - \phi_a(t, x))^2} \approx 2\Gamma_0 \Delta t. \qquad (27b)$$

The charges are updated in a similar way, with the extra difficulty that the noise term generated by the updates must be a total divergence. This is tackled by updating the lattice cells in pairs, making a Metropolis proposal for the charge transfer between two cells—see Appendix A.

Using a Metropolis update to solve for the nonideal part of the dynamics has several advantages over a direct time evolution of the Langevin process. For instance, it allows us to design a scheme whose equilibrium properties are independent of the time stepping. It also allowed us to use larger time steps compared to a naive discretization of the equations of motion. The numerical code is implemented with PETSC and MPI [36,37].

III. STATICS

A. Thermodynamics

Our goal in this section is to fix the static nonuniversal parameters of the model from its thermodynamics.

---

[3]In the sphaleron case the timescales between the metropolis and Langevin times must be carefully matched. In the current simulations, which are near the critical point of the model, this matching is unnecessary, as the lattice units and bare parameters are always adjusted to reproduce the pion pole frequency and width—see Sec. II B.

The magnetization of the system is an average over the volume at a given time moment:

$$M_a(t) \equiv \frac{1}{V}\sum_x \phi_a(t, x), \qquad (28)$$

and its time average, denoted with $\langle \ldots \rangle$, determines the condensate $\bar{\sigma}$

$$\bar{\sigma} \equiv \langle M_0 \rangle. \qquad (29)$$

At infinite volume, the dependence of the condensate on the temperature and magnetic field takes the scaling form given in (12). The nonuniversal constants m_c^2, H_0, $\mathfrak{m}^2$ are fit to our numerical data on $\bar{\sigma}$. We first determine m_c^2, then we simulate on the critical line with $m_0^2 = m_c^2$ to determine H_0, and finally, we simulate at $H = 0$ to find $\mathfrak{m}^2$. Anticipating the results of this section, we obtain with $\lambda = 4$

$$m_c^2 = -4.8110(4), \quad H_0 = 5.15(5), \quad \text{and} \quad \frac{\mathfrak{m}^2}{|m_c^2|} = 1.03(2). \qquad (30)$$

Following standard technique [38], we determined the critical coupling of the model m_c^2 by measuring Binder cumulants and determining when they cross a nominal value, which was taken from previous simulations [39]. Further details are given in Appendix B 1.

To determine H_0 we made a scan on the critical line, i.e., setting $T = T_c$ and scanning the magnetic field H. The details are presented in Appendix B 2. The data for $\bar{\sigma}$ on $32^3 64^3$ lattices on the critical line are shown in the left panel of Fig. 1. They were fit to a finite-size functional form given by Engels and Karsch [6], which fixes the value of H_0 given in (30), and quantifies finite-size corrections. The fit is reasonable and has $\chi^2/\text{dof} = 2$. The magnetization at infinite volume from the results of this fit is shown by the dashed line. We see that already at $L = 64$ we are essentially at infinite volume for the range of H considered in this work. Our dynamical simulations in Sec. IV are all done with $L^3 = 80^3$. This analysis on the critical line suggests that finite-volume corrections are modest.

In the next step we performed simulations at $H = 0$ with $T < T_c$, in order to fix the nonuniversal constant $\mathfrak{m}^2$. Details are presented in Appendix B 3. The infinite-volume magnetization Σ at zero field is defined as

$$\Sigma \equiv \lim_{H \to 0^+} \lim_{L \to \infty} \bar{\sigma}. \qquad (31)$$

Extracting the magnetization Σ is difficult as, in any finite volume,

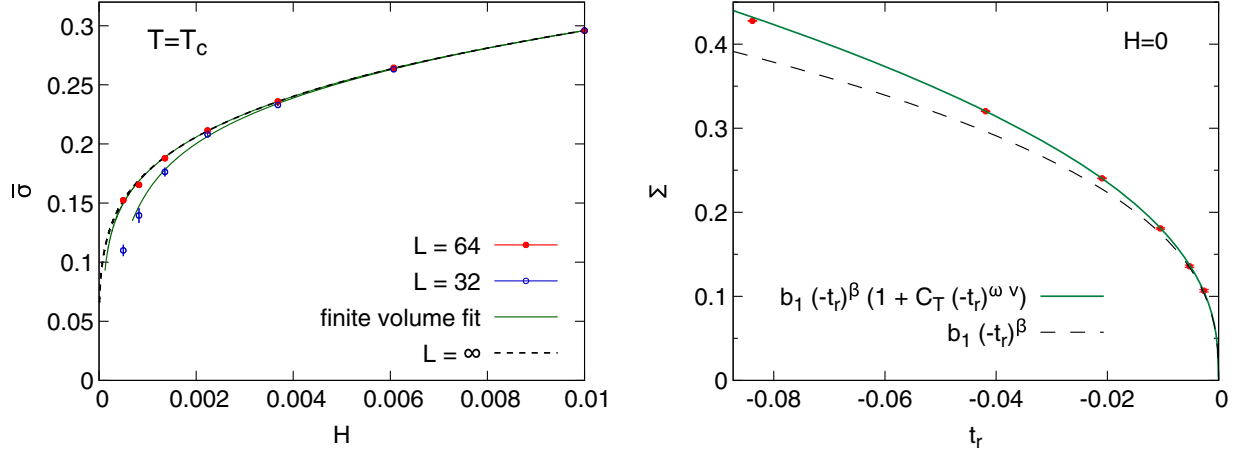$$\lim_{H \to 0} \bar{\sigma}|_{L\,\text{fixed}} = 0. \qquad (32)$$

FIG. 1. (Left) $\bar{\sigma}$ on the critical line for $L = 32$ and $L = 64$ together with a finite-volume fit to the data, which determines the nonuniversal parameters H_0, L_0 and C_H. The fit form is taken from Engels and Karsch [6] [see text surrounding Eq. (B6)]. Also shown are the results of the fit at $L = \infty$. (Right) Extracted infinite volume expectation value, $\Sigma \equiv \lim_{H \to 0^+} \lim_{L \to \infty} \bar{\sigma}$, as a function $t_r \equiv (m_0^2 - m_c^2)/|m_c^2|$. The fits and extraction procedure are discussed in the text. Also shown is the fit result without the subleading correction.

This is because when $H\Sigma V \sim 1$, the orientation of magnetization vector M_a begins to wander on the group manifold, averaging to zero in the limit of zero external magnetic field. One way to extract Σ is to look at the fluctuations of M_a, evaluating $\langle M^2 \rangle = \langle M_a M_a \rangle$, which is approximately Σ^2 at large volume. The leading deviation of $\langle M^2 \rangle$ and Σ^2 at finite volume comes from the fluctuations of long-wavelength Goldstone modes, and can be neatly analyzed with a Euclidean pion EFT [40]. We detail these corrections, which were essential to a reliable extraction of $\Sigma(T)$, in Appendix B 3.

Our results for $\Sigma(T)$ are shown in the right panel of Fig. 1, and are fit with the functional form

$$\Sigma = b_1(-t_r)^\beta (1 + (-t_r)^{\omega\nu} C_T). \tag{33}$$

with critical exponents β and δ from [6] and ω from [39]. Here we are using

$$t_r \equiv \frac{m_0^2 - m_c^2}{|m_c|^2}, \tag{34}$$

instead of $\bar{t}_r$, and we defined $b_1 \equiv (|m_c^2|/\mathfrak{m}^2)^\beta$. The second term in (33) captures the first subleading correction to scaling.

Our fit to $\Sigma(T)$ is shown in the right panel of Fig. 1 and yields $b_1 = 0.544(4)$ and $C_T = 0.20(2)$ with a $\chi^2/\text{dof} = 1.4$. We have excluded the largest value of $(-t_r)$ from the fit. For comparison, we also show the fit results for the first term $b_1(-t_r)^\beta$. Clearly, for precision work the subleading corrections are important in the temperature range we are considering. The parameter b_1 determines the scale $\mathfrak{m}^2$ described earlier (i.e., $\mathfrak{m}^2 = |m_c^2| b_1^{-1/\beta}$) yielding the results presented in (30).

To summarize, in this section we have established the nonuniversal parameters m_c^2, H_0, and $\mathfrak{m}^2$ which determine the map between the model and the conventionally parametrized $O(4)$ critical point. The results are given in (30).

B. The static pion EFT and Gell-Mann-Oakes-Renner

Before turning to the dynamics we will determine the validity of the Euclidean pion EFT referred to above, relegating all details to Appendix B 4. At all temperatures, $O(4)$ symmetry guarantees that the transverse susceptibility is determined by the condensate $\bar{\sigma}$:

$$\chi_\perp = \lim_{k \to 0} G_{\pi\pi}(k) = \frac{\bar{\sigma}}{H}, \tag{35}$$

where $G_{\pi\pi}(k)$ is the static correlation function. At low temperatures the magnitude of the condensate $\sqrt{\phi^2}$ is approximately frozen to $\bar{\sigma}$, and the long-wavelength order parameter fluctuations are determined by the fluctuations in the phase φ, $\pi_s(x) \simeq \bar{\sigma}\varphi_s(x)$. The static action for the Gaussian effective theory describing the phase fluctuations takes the form [29,41]

$$S_E = \int d^3x \frac{1}{2} f^2 \nabla\vec{\varphi} \cdot \nabla\vec{\varphi} + \frac{1}{2} f^2 m^2 \vec{\varphi}^2, \tag{36}$$

and makes a definite prediction for the static correlator:

$$G_{\pi\pi}(k) = \frac{\bar{\sigma}^2}{f^2} \frac{1}{k^2 + m^2}, \tag{37}$$

where f^2 is the decay constant and m is the screening mass. Comparing the predicted correlator to the susceptibility yields the Gell-Mann-Oakes-Renner (GOR) relation:
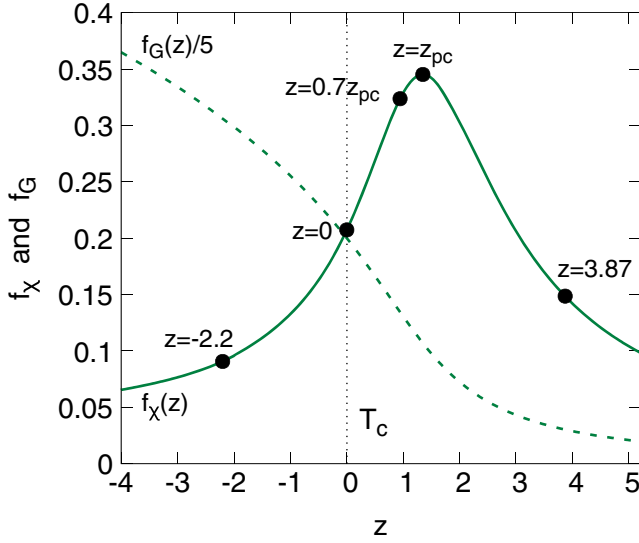
FIG. 2. A parametrization of the longitudinal susceptibility $\chi_\parallel \propto f_\chi(z)$ and mean magnetization $\bar{\sigma} \propto f_G(z)$ taken from the simulations of Engels and Karsch [6]. The black points are the z values which will be simulated in this work. Further simulation details are given in Fig. 3.

$$f^2 m^2 = H\bar{\sigma}. \tag{38}$$

At a finite negative z, the GOR relation is only approximate, receiving corrections due to fluctuations of the σ field. We have fit the static $\pi\pi$ correlator to find the decay constant f^2 and the screening mass m^2 at a nominal point in the broken phase, $z = -2.2011$ and $H = 0.003$ (see Fig. 2). Comparing $f^2 m^2$ to $H\bar{\sigma}$ yields

$$\frac{f^2 m^2}{H\bar{\sigma}} = 1.006 \pm 0.007 (\text{stat.}). \tag{39}$$

Evidently, already at $z = -2.2$, the Euclidean pion EFT works to better than a percent.

Having studied the statics of the pions, in the next section we will turn to the dynamics, making use of these results in Sec. IV C.

IV. DYNAMICS

A. The simulations

To get an overview of the phase diagram, in Fig. 2 we show the scaling function of the magnetization $f_G(z)$ and the corresponding function for longitudinal susceptibility f_χ [6]:

$$\chi_\parallel = \frac{\partial\bar{\sigma}}{\partial H} = \frac{h^{1/\delta-1}}{H_0} f_\chi(z). \tag{40}$$

The susceptibility shows a prominent maximum at the pseudocritical point with z value of $z_{\text{pc}} \simeq 1.35$. In order to scan the dynamics of the transition, we have performed real-time simulations at the black points. We also made a scan on the critical line $z = 0$ for various values of the magnetic field. The dynamical parameters as well as the run times and other information are gathered in Fig. 3. Additional details on how the temporal correlations functions are computed and Fourier analyzed are presented in Appendix A 2 d.

B. Overview

We will start by presenting an overview of the critical dynamics as the temperature is scanned across the phase transition. At high temperatures, the order parameter is small and simply dissipates through the damping term in the equations of motion. Since there is no preferred direction, the longitudinal and transverse order parameters excitations, σ and $\vec{\pi}$, are nearly degenerate. In the vector channel, the total charge is constant in time and the dissipation affects only nonzero Fourier modes, which are not studied here. The situation is different in the axial channel, since the axial charge is not conserved. However, the explicit symmetry-breaking term in the action, $H\sigma$, is

FIG. 3. Overview of the different simulations used in this work. In all cases, $\chi_0 = 5$, $\Gamma_0 = 1$, $D_0 = \frac{1}{3}$. The simulations are run on a lattice of volume $V = 80^3$ for 10^6 time steps (see Appendix A for a discussion of the algorithm and the size of the steps). The first 10^4 are discarded to ensure the system has thermalized.

tiny, since it is proportional to the magnetic field H (or quark mass) and the order parameter, which is small at high temperatures, $\bar{\sigma} \propto H$. As a result, the axial charge will dissipate rather slowly over a timescale of order $H\bar{\sigma}/\chi_0 \propto H^2$. In this regime, the dynamics of the axial charge is unrelated to the pions. However, as we lower the temperature, the order parameter acquires an H-independent expectation value, and the axial channel gets modified; the order parameter field and the axial charge are now entangled. In the deeply broken phase at low temperatures, the axial charge and the transverse part of the field will no longer just dissipate. Indeed, their dynamics become intrinsically locked, and they acquire the quasiparticle characteristics of the Goldstone modes associated with the broken symmetry. By contrast, in this regime the longitudinal excitation of the order parameter (the σ)

has a large mass and its dynamics remains purely dissipative.

These qualitative behaviors are precisely observed in our data. In Fig. 4, we start by showing the results of a simulation performed in the unbroken phase, $z = 3.87$. In the left plot we show the statistical correlator for the σ, π, and axial channels as a function of time. Noting that the x axis is on a logarithmic scale, the slow dissipation in the axial channel is apparent. It is also apparent that the σ and π channels are almost degenerate and dissipate on a much shorter timescale. This is also clearly seen in the corresponding Fourier transforms (right), where σ and π correlators appear as a single dissipative peak, which is much broader than corresponding peak in the axial correlator.

In Fig. 5, we show the behavior of the axial charge correlator at the pseudocritical and critical temperatures, and
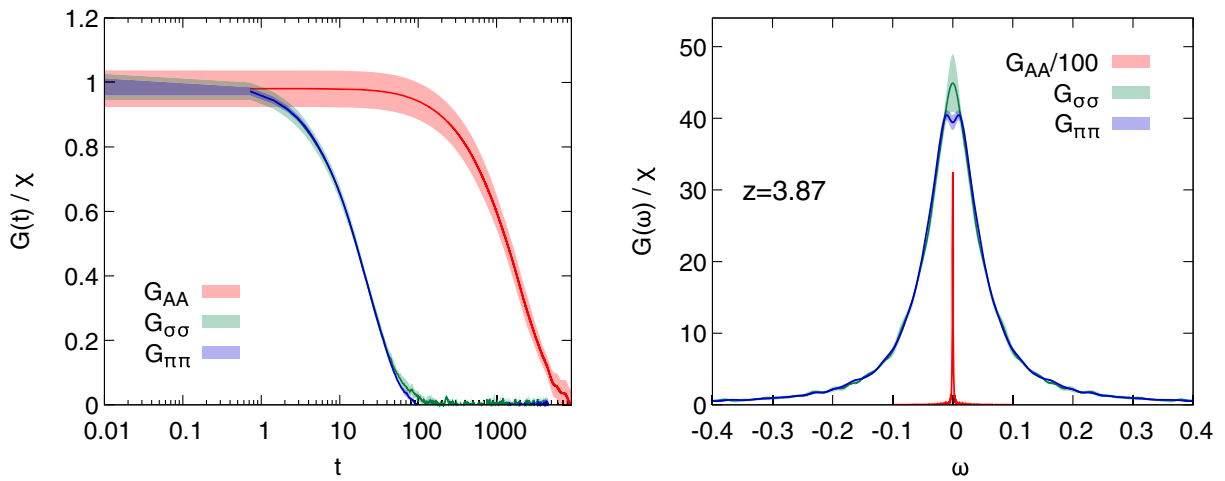

FIG. 4. (Left) Statistical correlation functions in the unbroken phase as a function of time for the axial charge, σ, and π. In this regime the σ and π channels become degenerate, and the axial charge is almost conserved. The logarithmic x axis emphasizes that the relaxation time of the axial charge is orders of magnitude longer than the one of the σ and π. (Right) The corresponding correlators as a function of frequency.
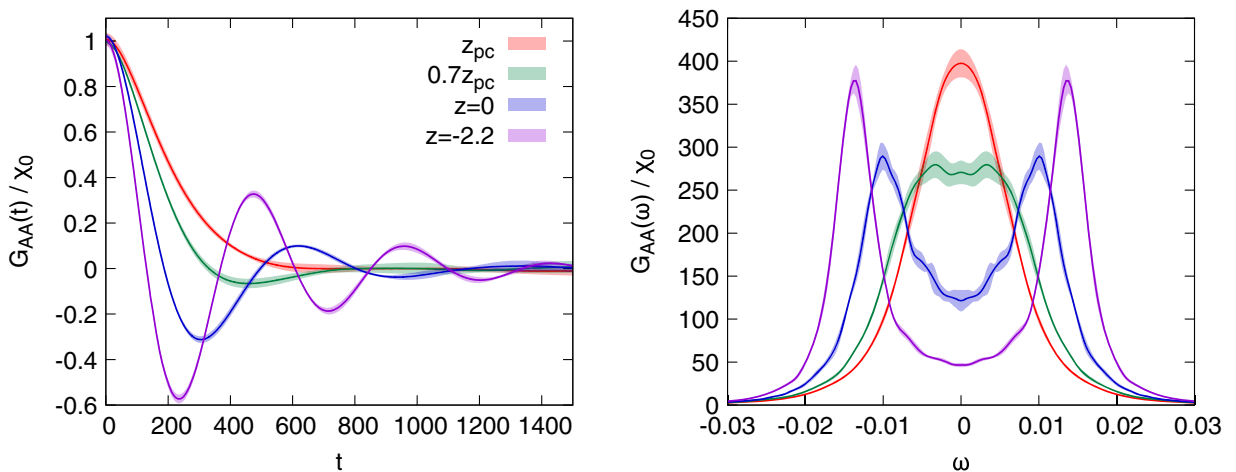

FIG. 5. (Left) The axial charge correlator as a function of time with z spanning the phase transition. (Right) The corresponding correlators in the frequency domain.
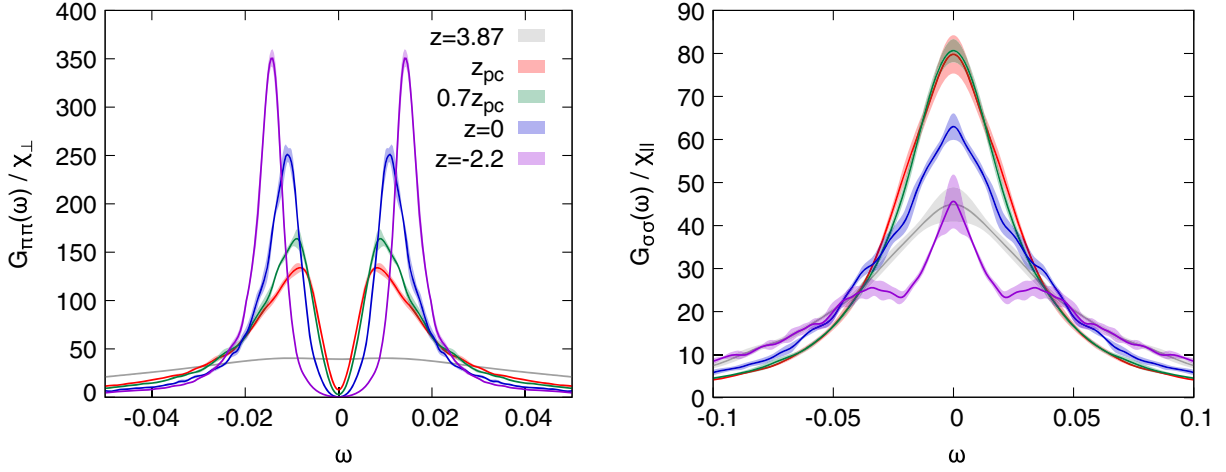
FIG. 6. (Left) The Fourier transform of the $\pi\pi$ correlator with z spanning the phase transition. (Right) The corresponding $\sigma\sigma$ correlators. Note the different scales used in the two panels. In particular, the gray curves in the left and right panels are almost identical, as shown in Fig. 4.

at lower temperatures, in the broken phase. In the left panel, we show the correlation functions as a function of time, while in the right panel we show their Fourier transforms. At the pseudocritical temperature (the red curves), the axial charge correlator is still purely dissipative, but the peak is much broader than in Fig. 4, indicating that the charge is no longer approximately conserved. As we lower the temperature to T_c (the blue curves), we start seeing the emergence of propagating pions, which appear as oscillations in the correlator as a function of time, or equivalently, as quasiparticle peaks in the Fourier transform. At the critical temperature there are no drastic changes (this is expected in a finite magnetic field), and the correlator behaves as it does in the broken phase, with propagating pions which are clearly visible in the axial channel. As one moves further into the broken phase (the purple curves), the pion peaks become increasingly separated, and the real-time pion EFT discussed below becomes valid (see Sec. IV C).

It seems that around the pseudocritical temperature z_{pc} (the red curve) the axial charge propagator starts changing its behavior from purely dissipative to quasiparticlelike. Indeed, at $z = 0.7z_{\mathrm{pc}}$ (the green curve), i.e., slightly below the pseudocritical point, the dissipative peak is already quite deformed, which reflects the nascent formation of the two quasiparticle peaks.

In the left and right panels of Fig. 6, we show the corresponding statistical correlators for the π and σ fields as a functions of frequency, with z spanning the phase transition. In the deeply unbroken phase the two channels are mostly indistinguishable (the gray bands), as pointed out before. Lowering the temperature to the pseudocritical point, the pseudoscalar channel acquires a double-peak structure, while the scalar channel remains purely dissipative. Going further down in temperature, the quasiparticle peaks in the pseudoscalar channel separate. Interestingly at z_{pc}, the pion correlator already has a quasiparticle peak,

while the axial charge correlator is still dissipative (Fig. 5); only past the pseudocritical point do their correlation functions become closely related.

C. Broken phase: Pion EFT

Deep in the broken phase, the fluctuations of the order parameter are dominated by the phase fluctuations $\pi_s(t, x) \simeq \bar{\sigma}\varphi_s(t, x)$, which are tightly correlated to the axial charge fluctuations through the Josephson constraint, $\partial_t \vec{\varphi} \simeq \vec{\mu}_A$. The dissipative hydrodynamic theory for the phase fluctuations has been worked out in [16,17,29], and provides a real time analog of the static Gaussian effective theory described in Sec. III B.

The linear response of hydrodynamic theory has been analyzed in [18,29], and the hydrodynamic prediction for the dynamical correlators in the $\boldsymbol{k} = 0$ case is

$$G_{\pi\pi}(\omega) = \frac{2\chi_\perp \Gamma m^2 \omega^2}{(-\omega^2 + m_p^2)^2 + \omega^2(\Gamma m^2)^2}, \qquad (41)$$

$$G_{AA}(\omega) = \frac{2\chi_0 \Gamma m^2 m_p^2}{(-\omega^2 + m_p^2)^2 + \omega^2(\Gamma m^2)^2}. \qquad (42)$$

Here m_p^2 is the pole mass of the pion excitation, m is the transverse static screening mass, Γ is a dissipative coefficient correcting the Josephson constraint, and finally χ_0 and $\chi_\perp$ are the appropriate static susceptibilities, which are required to normalize these expressions:

$$\int \frac{\mathrm{d}\omega}{2\pi} G_{\pi\pi}(\omega) = \chi_\perp, \qquad (43)$$

$$\int \frac{\mathrm{d}\omega}{2\pi} G_{AA}(\omega) = \chi_0. \qquad (44)$$

The fact that the pions are pseudo-Goldstone bosons, and correspondingly that the axial current is partially conserved (PCAC), leads to the well-known and remarkable property that the dynamical pole mass m_p can purely be computed from the static properties discussed in Sec. III B. In particular, at low-enough temperatures, we have a finite-temperature GOR relation [29,30,42]:

$$m_p^2 = v^2 m^2 = \frac{H\bar{\sigma}}{\chi_0}, \tag{45}$$

where $v^2 \equiv f^2/\chi_0$ is the pion velocity.

Already in Fig. 5 we saw the appearance of pion excitations. We will now try to assess the validity of the pion EFT. To do so, we attempt to fit expressions (41) and (42) from our statistical correlators. To perform these fits, we first fix the normalizations by extracting from our data the susceptibilities, χ_0 and $\chi_\perp$. We then use a two-parameter model, involving m_p and $\Gamma_p = \Gamma m^2$, and simultaneously fit the statistical correlators in the π and axial channels.

Results of these fits are shown in Fig. 7, yielding parameters

$$m_p = (1.4387 \pm 0.0005(\text{stat.})) \times 10^{-2}, \tag{46}$$

$$\Gamma_p = (5.088 \pm 0.005(\text{stat.})) \times 10^{-3}, \tag{47}$$

$$\chi^2/\text{dof} = 1.93. \tag{48}$$

Although the width is still pretty large, $\Gamma_p/2m_p \simeq 0.17$, we find good agreement between the numerical data and the pion EFT, with only small noticeable deviations around the maxima of the two-point functions.

This extraction of the pole mass allows us to verify the dynamical part of the GOR relation. Referring the reader again to Sec. III B for the corresponding extraction of the static quantities, we find

$$\frac{H\bar{\sigma}}{\chi_0} \cdot \frac{1}{m_p^2} = 1.011 \pm 0.001(\text{stat.}). \tag{49}$$

We see again that already at $z = -2.2$, the deviations from GOR are remarkably small, of order 1%, which could be due to corrections of order $\sim(\Gamma_p/2m_p)^2$. Note also that part of this 1% deviation could be due to some remaining systematic errors in our time evolution; see Appendix A 2 a for more details.

D. Critical line: Dynamical scaling

Moving on to the critical line $z = 0$, we consider the scaling of the critical dynamics. Focusing on $\vec{k} = 0$ modes and recalling that the (e.g., longitudinal) correlation length scales as

$$\xi = \xi_c H^{-\nu_c}, \tag{50}$$

on the critical line, the "dynamic scaling hypothesis" (11a)–(11c) gives us the following scaling forms for the correlators on the critical line:

$$\frac{G_{\sigma\sigma}(t,H)}{\chi_\parallel} = Y_\sigma^c(H^{\zeta\nu_c}t), \tag{51}$$

$$\frac{G_{\pi\pi}(t,H)}{\chi_\perp} = Y_\pi^c(H^{\zeta\nu_c}t), \tag{52}$$

$$\frac{G_{AA}(t,H)}{\chi_0} = Y_A^c(H^{\zeta\nu_c}t), \tag{53}$$

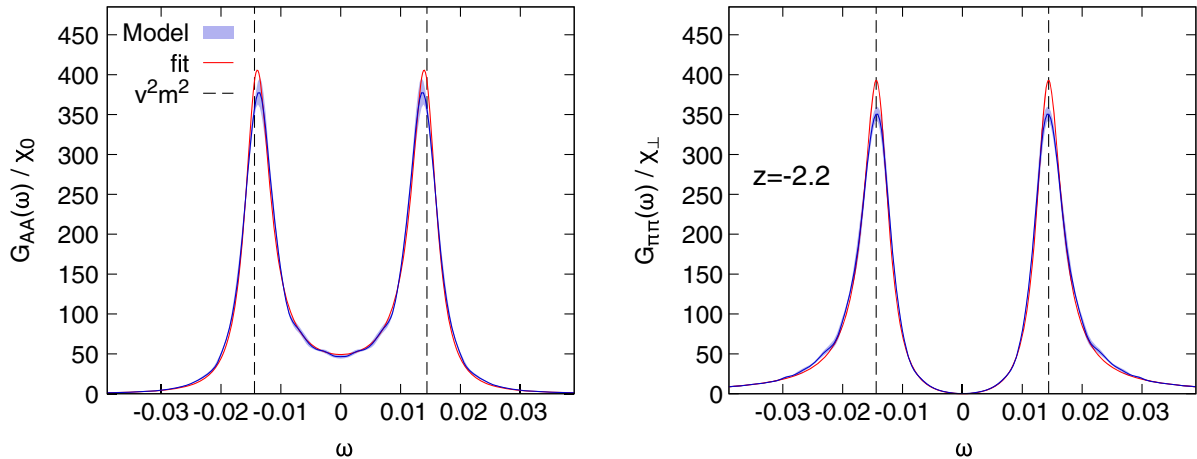with for example, $Y_A^c(H^{\zeta\nu_c}t) = Y_A(\Omega\xi^{-\zeta}t, 0, 0)$.

FIG. 7. Statistical correlators for the π and axial channels together with the result of a global fit to the functional form from the chiral hydrodynamic theory (see text). The fitted parameters are $m_p = (1.4387 \pm 0.0005(\text{stat.})) \times 10^{-2}$ and $\Gamma_p = (5.088 \pm 0.005(\text{stat.})) \times 10^{-3}$, with a χ^2/dof of 1.93.
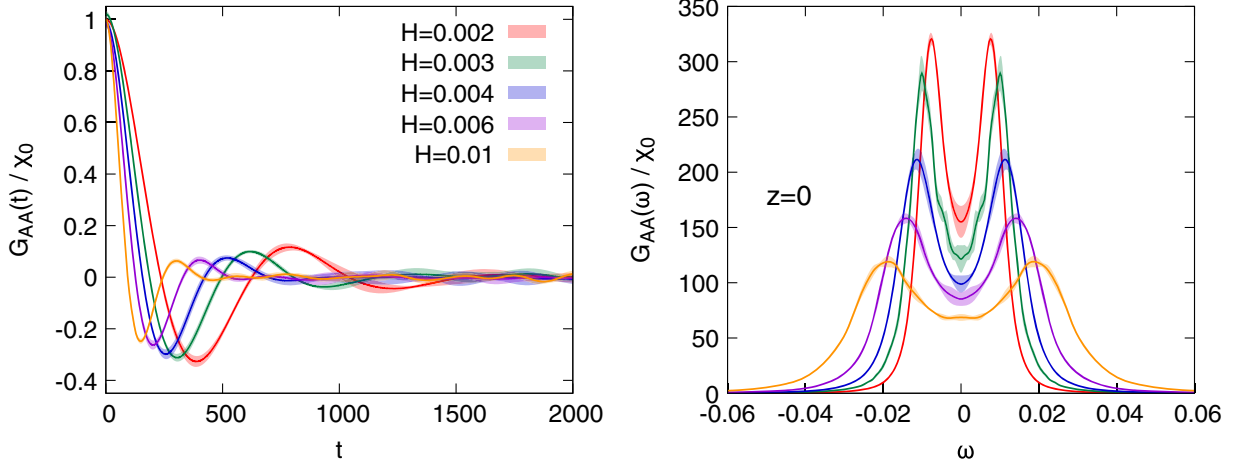
FIG. 8. (Left) Time-dependent axial charge correlation functions for different magnetic fields on the critical line, $z = 0$. (Right) Corresponding statistical correlator in frequency space.

To verify the validity of the hypothesis and to determine the dynamical exponent ζ, we studied a set of simulations at $m_0^2 = m_c^2$ for $H = 0.002, 0.003, 0.004, 0.006, 0.01$. We present the results obtained for the axial-axial channel in Fig. 8. The left plot shows the time-dependent correlator $G_{AA}(t)$ for the different magnetic fields, while the right panel displays its corresponding Fourier transform $G_{AA}(\omega)$. Qualitatively at least the curves show a scaling behavior.

To quantitatively assess the scaling ansatz (53) and to extract the exponent ζ from our data, we located the time when $G_{AA}(t, H)$ reaches its first minimum, $t_{\min}(H)$, which can be determined with reasonable accuracy. From the scaling ansatz, we see that, given two magnetic fields H_1, H_2, we expect

$$\frac{t_{\min}(H_2)}{t_{\min}(H_1)} = \left(\frac{H_1}{H_2}\right)^{\zeta \nu_c}. \tag{54}$$
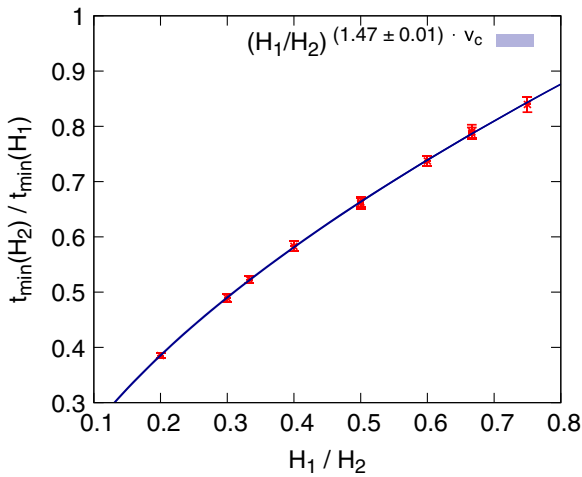
We show this ratio as a function of H_1/H_2 in the left panel of Fig. 9. The data are well described by the power-law form, and we obtain a nominal value for the dynamical exponent of

$$\zeta_{\rm fit} = 1.47 \pm 0.01, \tag{55}$$

taking $\nu_c = 0.4024$ from [6].

With an estimate of the critical exponent in hand, we can verify the ansatz (53). Indeed by appropriately rescaling times and frequencies, we expect to see our correlators $G_{AA}(t, H)$ and spectral function

$$\rho_{AA}(\omega, H) = \omega G_{AA}(\omega, H), \tag{56}$$

collapse to a single curve. The scaling of $G_{AA}(t, H)$ is shown in the right panel of Fig. 9, while the scaling
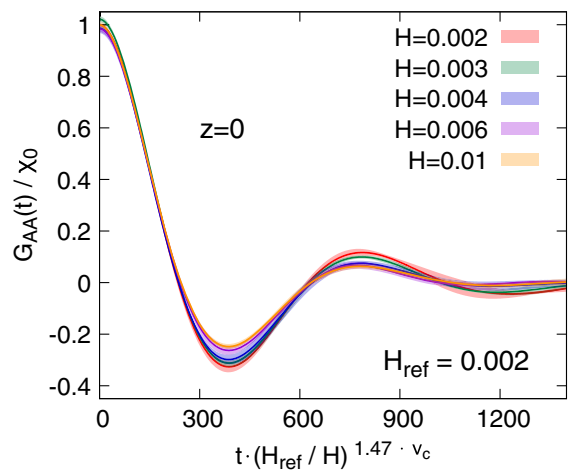

FIG. 9. (Left) Ratios, $t_{\min}(H_2)/t_{\min}(H_1)$, extracted from the first minima of Fig. 8 as a function of H_1/H_2 (see text). On the critical line, we expect this ratio to be described by a universal critical exponent $t_{\min}(H_2)/t_{\min}(H_1) = (H_1/H_2)^{\zeta \nu_c}$. Our best fit gives $\zeta = 1.47 \pm 0.01$. (Right) Time-dependent axial correlation functions as a function of an appropriately rescaled time variable.
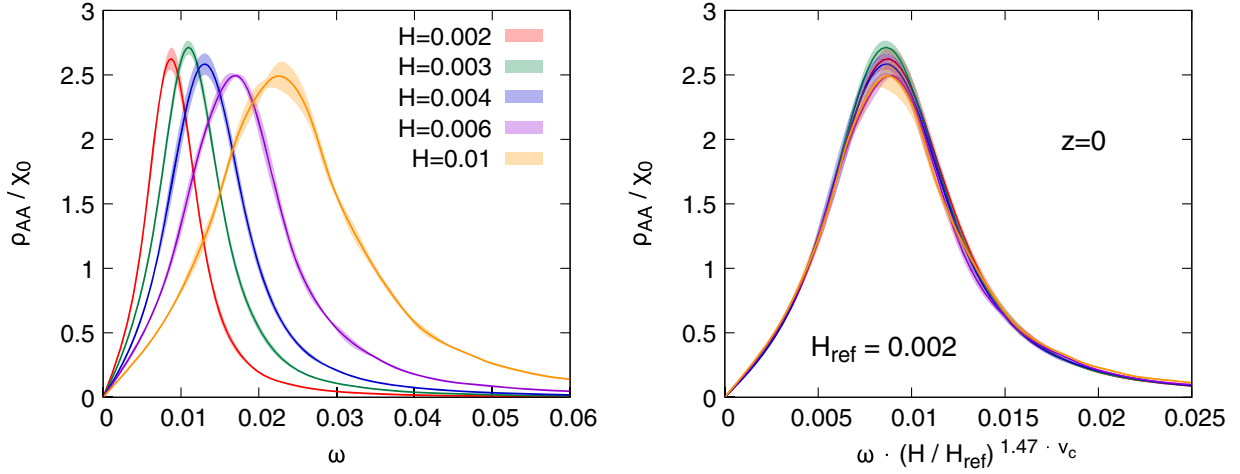
FIG. 10. (Left) Axial charge spectral function on the critical line. (Right) Axial spectral function as a function of an appropriately rescaled frequency variable. In both cases, we see the expected data collapse.

$\rho_{AA}(\omega, H)$ is shown in Fig. 10. To obtain this data collapse, we have rescaled the time and inverse frequency by $(H_{\text{ref}}/H)^{\zeta_{\text{fit}}\nu_c}$ with $H_{\text{ref}} = 0.002$.

Dynamical scaling is also expected to hold in the other channels and in particular we expect the same ζ_{fit} to govern the dynamics in the σ channel. This indeed happens, which we illustrate in Fig. 11 by showing the $\sigma\sigma$ correlator (left) and the corresponding collapsed spectral function (right).

Before moving on, let us emphasize that our numerical estimate of the critical dynamical exponent is close to the critical scaling prediction [2,23], $\zeta = d/2$. Considering, for example, the small violations of scaling seen in Fig. 9, we do not consider the deviation of ζ_{fit} from $d/2$ to be significant.

V. DISCUSSION

In this work, we numerically studied the universal critical dynamics relevant to two-flavor QCD close to

the chiral phase transition. More precisely, we simulated the dynamics of an $O(4)$ antiferromagnet, model G of [2,23]. After reviewing the model and explaining our conventions in Sec. II, we performed some "scale setting" in Sec. III, where we studied the thermodynamic properties of the model and extracted the relevant nonuniversal constants. We also determined some of the static properties of pions in the broken phase such as their screening masses and decay constants.

With these data in hand, we moved on to the main section of this work, Sec. IV, which studied the dynamics. Focusing on correlators at zero spatial momentum, we first performed a scan in temperature across the phase transition. We qualitatively confirmed that the dynamics takes place as expected, by studying the real-time correlation functions in the $\sigma\sigma$, $\pi\pi$ and axial-axial channels. At high temperature, the σ and π are degenerate and the axial charge is almost conserved. In the broken phase, the σ
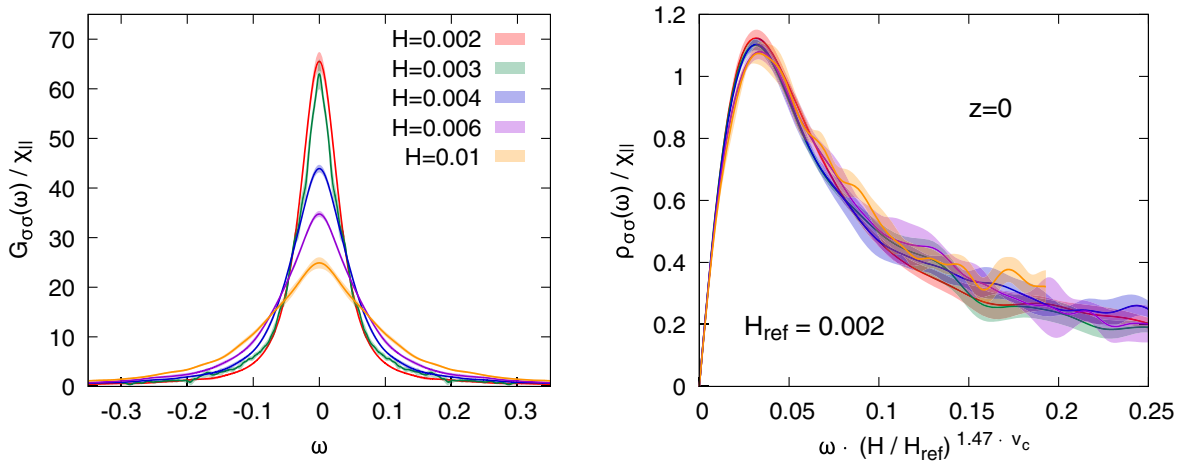

FIG. 11. (Left) Statistical correlator in the σ channel, on the critical line. (Right) Corresponding spectral function as a function of rescaled frequencies. The estimated critical exponent used for the rescaling is determined from the axial channel. The dynamical scaling hypothesis is satisfied and we observe a collapse of the different curves.

remains purely dissipative, while the π propagates and carries axial charge. In particular, we were able to observe that the coupling of the π to the axial charge precisely happens in the vicinity of the pseudocritical point, z_{pc}, defined as the line in the phase diagram where the static susceptibility peaks. This observation is yet another link between the static and dynamical properties of this critical model.

We also performed a quantitative study of the pion properties in the broken phase. We were able to fit the dynamical correlator to a particle resonance ansatz predicted by the chiral hydrodynamic effective theory, and extract the pole mass and decay width. Furthermore, we verified that the Gell-Mann-Oakes-Renner relation, which relates the dynamical pole mass of the pions to their static screening mass, holds at the subpercent level. Last but not least, we performed a set of simulations along the critical line and extracted the dynamical critical exponent $\zeta = 1.47 \pm 0.01 \text{(stat.)}$, very close to the critical scaling prediction $\zeta = 1.5$ [2].

The numerical determination of ζ can be considered as a first step towards a complete quantitative characterization of the dynamics of the $O(4)$ antiferromagnet. Such a characterization would include additional studies at finite spatial momentum as in [27], and a more complete investigation of the dynamics in the chiral limit at finite volume with an appropriate real-time EFT. (The corresponding finite volume static EFT was written down long ago [40], and was helpful in the thermodynamic analysis in Appendix. B 3.) In order to use the model to analyze heavy-ion data as discussed in [17,18], it will be important to analyze the critical $O(4)$ dynamics for an expanding fluid, which introduces a rich hierarchy of scales. Finally, it will be interesting to apply the algorithm presented in Appendix A to other stochastic and critical systems.

ACKNOWLEDGMENTS

APPENDIX A: THE MODEL ON THE LATTICE

1. Relating lattice units to QCD

Continuing the discussion of Sec. II B, our goal is to fix the spatial cutoff a in units of meters, so that the model will reproduce the physical correlation length. In the computer code the cutoff is the lattice spacing, and is set to unity. Similarly the times are measured in units of $1/(g_0 T_c)$, and we will set the g_0 in physical units so that the model reproduces the pion pole frequency. The results of this section are summarized by Eq. (20).

For any critical system with canonically normalized magnetic Hamiltonian $\Delta H = \int d^3 x H \sigma$, and mean order parameter of the form $\bar{\sigma} = B h^{1/\delta} f_G(z)$ with $h = H/H_0$, the combination of parameters $H_0 B/T_c$ has dimensions $(\text{length})^{-d}$ and defines a nonuniversal length:

$$(\xi_1)^{-d} \equiv \frac{H_0 B}{T_c}. \tag{A1}$$

The longitudinal correlation length of the generic critical system takes the form

$$\xi = \xi_1 h^{-\nu_c} f_\xi(z), \tag{A2}$$

where $f_\xi(z)$ is a universal function, including its normalization.[4]

In the $O(4)$ model where

$$H_0^{O(4)} = \sqrt{T_c/a^{d+2}} \, \hat{H}_0, \quad \text{and} \quad B^{O(4)} = \sqrt{T_c/a^{(d-2)}}, \tag{A3}$$

the length scale ξ_1 evaluates to

$$\xi_1^{O(4)} = a \hat{H}_0^{-1/d}. \tag{A4}$$

In QCD we have $\xi_1^{\text{QCD}} = (H_0^{\text{QCD}} B^{\text{QCD}}/T_c)^{-1/d}$, leading to the identification given in the text:

$$a = \hat{H}_0^{1/d} \xi_1^{\text{QCD}}. \tag{A5}$$

---

[4]The function $f_\xi(z)$ for the longitudinal correlation length is proportional to $\hat{g}_\xi^L(z)$ of [41], with the proportionality constant given by universal amplitude ratios. With some patience, one finds $f_\xi(z) = (Q_c R_\chi)^{1/d} (Q_2^L/\delta R_\chi)^{\nu/\gamma} \hat{g}_\xi^L(z)$.

Next we discuss the dynamics. There is a timescale set by the frequency of the pion pole[5]

$$(m_p^{\text{QCD}})^2 \equiv \frac{1}{\hbar^2} \frac{m_q c^2 \langle \bar{q}q \rangle}{\chi_0}, \tag{A8}$$

$$= \frac{H_0^{\text{QCD}}}{\hbar^2} \frac{h \langle \bar{q}q \rangle}{\chi_0}, \tag{A9}$$

In the $O(4)$ model it is easy that the corresponding frequency in physical units is

$$m_p^2 = \frac{g_0^2 H \bar{\sigma}}{\chi_0} = g_0^2 T_c \hat{H}_0 \left(\frac{h \hat{\bar{\sigma}}/a^3}{\chi_0} \right). \tag{A10}$$

Comparing the two expressions, using $\langle \bar{q}q \rangle = B^{\text{QCD}} \hat{\bar{\sigma}}$ and the identification

$$h = \frac{m_q c^2}{H^{\text{QCD}}} = \frac{\hat{H}}{\hat{H}_0}, \tag{A11}$$

leads to the result

$$g_0^2 = \frac{1}{\hbar^2}. \tag{A12}$$

Equations (A5) and (A12) are presented in the body of the text in Eq. (20).

2. Overview of the algorithm

In this section we will describe the updated algorithm in detail. We first discretize the fields on a spatial lattice (with lattice spacing $a = 1$) writing the effective Hamiltonian as

$$\mathcal{H} = \sum_{x,e_i} \frac{1}{2} (\phi(t, x + e_i) - \phi(t, x))^2 + \sum_x V(\phi(t, x))$$

$$- H\sigma(t, x) + \sum_x \frac{n^2(t, x)}{4\chi_0}. \tag{A13}$$

Here $x = (x_1, x_2, x_3)$ labels the lattice sites, and $e_i = e_1, e_2, e_3$ is a unit vector in the corresponding direction. Variational derivatives in the equations of motion get replaced by ordinary derivatives, $\delta \mathcal{H}/\delta \phi \to \partial \mathcal{H}/\partial \phi$, etc.

The equations of motion for $U \in [\phi_a, n_{ab}]$ can be written schematically:

---

[5]This formula assumes that the total charge operators Q_{ab} are unitless and satisfy the $O(4)$ commutation relations:

$$[Q_{ab}, Q_{cd}] = i(\delta_{ac} Q_{bd} + \delta_{bd} Q_{ac} - \delta_{ad} Q_{bc} - \delta_{bc} Q_{ad}). \tag{A6}$$

The susceptibility is defined by the averages

$$\langle Q_{ab} Q_{cd} \rangle = T\chi_0 V(\delta_{ac}\delta_{bd} - \delta_{ad}\delta_{bc}). \tag{A7}$$

$$\partial_t U = O_A(U) + O_B(U) + O_C(U). \tag{A14}$$

The first operator describes the evolution under the ideal equations of motion, while the second two operators describe the dissipative dynamics of the order parameter ϕ and the charges n_{ab} respectively. We will use operator splitting to solve for the total time evolution. The most straightforward procedure is to update the fields sequentially for a small period of time Δt:

$$U \overset{A}{\to} U \overset{B}{\to} U \overset{C}{\to} U. \tag{A15}$$

More explicitly we have:
  A Stage:

$$\partial_t \phi_a = -\mu_{ab} \phi_b, \tag{A16}$$

$$\partial_t n_{ab} = \partial_i(\phi_a \partial^i \phi_b - \phi_b \partial^i \phi_b) - (H_a \phi_b - H_b \phi_a), \tag{A17}$$

B Stage:

$$\partial_t \phi_a = -\Gamma_0 \frac{\delta \mathcal{H}}{\delta \phi_a} + \theta_a, \tag{A18}$$

$$\partial_t n_{ab} = 0, \tag{A19}$$

C Stage:

$$\partial_t \phi_a = 0, \tag{A20}$$

$$\partial_t n_{ab} = \sigma_0 \nabla^2 \frac{\delta \mathcal{H}}{\delta n_{ab}} + \partial_i \Xi_{ab}^i. \tag{A21}$$

We will view each step as part of a Markov chain.

A technical complication is that the C step takes approximately six times longer than the B step, because there are many more random numbers to generate. The ideal step A also is about twice slower than the B step. So as a practical matter, for a complete step over a time Δt we will take the following updates:

$$ABB\,ABB\,ABB\,C, \tag{A22}$$

where the time increment for B is $\Delta t_B = \Delta t/6$ while the time step for A is $\Delta t_A = \Delta t/3$. An optimal time step thermalizes modes of order of the lattice spacing in a short period of wall time. We have found $\Delta t = 0.24/\Gamma_0$ is approximately optimal (see below) for the algorithm discussed here.

a. Ideal step

In order to perform our ideal step, let us first rewrite the ideal part of our continuous equation as follows:

$$\partial_t \phi_a = -\frac{n_{ab}}{\chi_0} \phi_b, \tag{A23}$$

$$\partial_t n_A^s = \partial_i(\sigma \partial^i \phi_s - \phi_s \partial^i \sigma) - H\phi_s, \tag{A24}$$

$$\partial_t n_V^s = \epsilon^{ss_1 s_2} \partial_i(\phi_{s_1} \partial^i \phi_{s_2}). \tag{A25}$$

Eq. (A23) makes it apparent that the ideal evolution of the order parameter is simply an $O(4)$ rotation by the currents. More explicitly, in the $O(4)$-algebra matrix notation, we have

$$\partial_t \phi = -\frac{i}{\chi_0} N\phi, \tag{A26}$$

with

$$N(t) = \vec{n}_A(t) \cdot \vec{K} + \vec{n}_V(t) \cdot \vec{J}, \tag{A27}$$

and $\vec{K}, \vec{J}$ the generators of $so(4)$

$$K_1 = -i\begin{pmatrix} 0 & 1 & 0 & 0 \\ -1 & 0 & 0 & 0 \\ 0 & 0 & 0 & 0 \\ 0 & 0 & 0 & 0 \end{pmatrix} \quad K_2 = -i\begin{pmatrix} 0 & 0 & 1 & 0 \\ 0 & 0 & 0 & 0 \\ -1 & 0 & 0 & 0 \\ 0 & 0 & 0 & 0 \end{pmatrix} \quad K_3 = -i\begin{pmatrix} 0 & 0 & 0 & 1 \\ 0 & 0 & 0 & 0 \\ 0 & 0 & 0 & 0 \\ -1 & 0 & 0 & 0 \end{pmatrix}, \tag{A28}$$

$$J_1 = -i\begin{pmatrix} 0 & 0 & 0 & 0 \\ 0 & 0 & 0 & 0 \\ 0 & 0 & 0 & 1 \\ 0 & 0 & -1 & 0 \end{pmatrix} \quad J_2 = -i\begin{pmatrix} 0 & 0 & 0 & 0 \\ 0 & 0 & 0 & -1 \\ 0 & 0 & 0 & 0 \\ 0 & 1 & 0 & 0 \end{pmatrix} \quad J_3 = -i\begin{pmatrix} 0 & 0 & 0 & 0 \\ 0 & 0 & 1 & 0 \\ 0 & -1 & 0 & 0 \\ 0 & 0 & 0 & 0 \end{pmatrix}. \tag{A29}$$

In particular, (A26) can be solved as

$$\phi(t + \delta t) = \exp\left(-\frac{i}{\chi_0}\int_t^{t+\delta t} dt' N(t')\right)\phi(t). \tag{A30}$$

With this in mind, before describing our time evolution, we need to discretize (A24) in space. For f and g functions evaluated on a discrete lattice, we discretize terms of the sort $\partial_x(g\partial_x f)$ in a straightforward way by integrating over finite-volume cells, e.g., in one dimension,

$$\frac{1}{a}\int_{x_{i-\frac{1}{2}}}^{x_{i+\frac{1}{2}}} dx \partial_x(g\partial_x f)$$

$$\simeq \frac{g|_{x_{i+\frac{1}{2}}}}{a^2}(f|_{x_{i+1}} - f|_{x_i}) - \frac{g|_{x_{i-\frac{1}{2}}}}{a^2}(f|_{x_i} - f|_{x_{i-1}})$$

$$\simeq \frac{1}{2a^2}[(g|_{x_{i+1}} + g|_{x_i})(f|_{x_{i+1}} - f|_{x_i})$$

$$\quad - (g|_{x_i} + g|_{x_{i-1}})(f|_{x_i} - f|_{x_{i-1}})], \tag{A31}$$

where we have approximated the value $g|_{x_{i+\frac{1}{2}}}$ at each interface as the mean of the central one, $g|_{x_{i+\frac{1}{2}}} = \frac{1}{2}(g|_{x_{i+1}} + g|_{x_i})$. Using the shorthand notation $f_{\pm i} \equiv f(t, x \pm e_i)$ leads us to define the following discrete evolution kernels:

$$\mathcal{K}_V^s = \frac{\epsilon^{ss_1 s_2}}{a^2}\sum_{i=1}^3(\pi_{s_1}\pi_{s_2,+i} - \pi_{s_1,-i}\pi_{s_2}), \tag{A32}$$

$$\mathcal{K}_A^s = -\pi_s H + \frac{1}{a^2}\sum_{i=1}^3(\sigma\pi_{s,+i} - \pi_s\sigma_{+i} - \sigma_{-i}\pi_s + \pi_{s,-i}\sigma). \tag{A33}$$

To evolve this system, we use a "position Verlet"-like symplectic integration. We start by computing Φ at half-integer steps, use it to evolve the currents by a time step δt and finish updating Φ by an extra half-time step, which gives

$$\phi\left(t + \frac{1}{2}\delta t\right) = \exp\left(-\frac{i}{\chi_0}\frac{\delta t}{2}N(t)\right)\phi(t), \tag{A34}$$

$$n_A^s(t + \delta t) = n_A^s(t) + \delta t \mathcal{K}_A^s, \tag{A35}$$

$$n_V^s(t + \delta t) = n_V^s(t) + \delta t \mathcal{K}_V^s, \tag{A36}$$

$$\phi(t + \delta t) = \exp\left(-\frac{i}{\chi_0}\frac{\delta t}{2}N(t + \delta t)\right)\phi\left(t + \frac{\delta t}{2}\right). \tag{A37}$$

A practical way to perform the rotations in (A34) and (A37) is to rewrite the $O(4)$ rotation as a direct product of $SU_L(2) \times SU_R(2)$ and to use the explicit form of the $SU(2)$ matrices for a given set of angles.

TABLE I. Accept-reject probability associated with our ideal step for different simulations.

z	H	Ideal accept probability, p
3.86978	0.003	0.958
1.34899	0.003	0.953
0.94429	0.003	0.951
0	0.002	0.948
0	0.003	0.948
0	0.004	0.948
0	0.006	0.947
0	0.01	0.946
−2.2011	0.003	0.940

The ideal evolution is associated with the conservation of the discretized energy, $\mathcal{H}$, for $\delta t \to 0$. Our symplectic evolution leads to a violation $\Delta E = \mathcal{H}(t + \delta t) - \mathcal{H}(t) \sim O(\delta t^2)$. One approach to this violation would be to just ignore it. Then the equilibrium action will be modified slightly by terms of order $O(\delta t^2)$ from (A13), shifting T_c by a small amount. We have seen indications of these shifts but have not explored this in detail. Instead we have added a Metropolis "accept-reject" step to the ideal evolution using $\min(1, \exp(-\Delta E))$ as the accept-reject probability. For our 80^3 lattices (which represent the majority of the simulations presented here) the reject probabilities are presented in Table I. The differences imply that the relative size of the dissipative and real parameters of the pions will weakly depend on δt.

The downside of having an acceptance probability p different from 1 is that it introduces a nontrivial renormalization of our time. Effectively, when the ideal step is rejected, the next dissipative step should be thought of as a way to generate a new candidate configuration for the ideal step; the clock freezes. The leading effect of a nonzero rejection probability for the ideal step can then be absorbed by rescaling Δt by the acceptance probability p. As a result, for all our simulations, the time variable we use is defined as

$$t = p n_{\text{steps}} \Delta t, \qquad (A38)$$

with the corresponding p read from Table I and Δt is the global time step of our algorithm.

As the results presented through this work support, this procedure allows us to faithfully correct our time variable. It is nonetheless true that it introduces some uncontrolled subleading systematic errors which may impede us from performing precision measurements in the future. This, together with the fact that the acceptance rate degrades for larger lattices, will lead us to use smaller ideal time steps for future simulations. It may also be worth investigating higher-order symplectic integrators, which would help to keep the reject probability small even for large volumes.

b. Viscous steps for ϕ

The spatially discretized equation to be solved is

$$\partial_t \phi_a = -\Gamma_0 \frac{\partial \mathcal{H}}{\partial \phi_a} + \theta_a, \qquad (A39)$$

where the noise correlator is given by a discretized Eq. (4a).

We will realize the Langevin process with Metropolis updates. Briefly, an update proposal is made for a lattice site x,

$$\phi_a(t + \delta t, x) = \phi_a(t, x) + \Delta \phi_a, \qquad (A40)$$

where for each flavor index a the increment is

$$\Delta \phi_a = \sqrt{2 \delta t \Gamma_0} \xi_0,$$

Here ξ_0 is a random number with unit variance $\langle \xi_0^2 \rangle = 1$. In practice ξ_0 is generated from a flat distribution between $[-\sqrt{3}, \sqrt{3}]$, since this is faster than generating Gaussian random numbers. The update proposal is accepted with probability $\min(1, e^{-\Delta H})$, where $\Delta \mathcal{H}$ is the change in the discretized Hamiltonian. If the proposal is rejected $\phi(t + \delta t, x) = \phi(t, x)$. For $\Delta \phi$ small,

$$\Delta \mathcal{H} \simeq \frac{\delta \mathcal{H}}{\delta \phi} \bigg|_{\phi_a(x,t)} \Delta \phi_a, \qquad (A41)$$

and then the mean and variance of the accepted proposals reproduce the dissipative and stochastic terms of the Langevin process:

$$\overline{\phi_a(t + \delta t, x) - \phi_a(t, x)} = -\delta t \Gamma_0 \frac{\delta \mathcal{H}}{\delta \phi} + \mathcal{O}(\delta t^2), \quad (A42a)$$

$$\overline{(\phi_a(t + \delta t, x) - \phi_a(t, x))^2} = 2 \delta t \Gamma_0 + \mathcal{O}(\delta t^2). \qquad (A42b)$$

For the sake of clarity, let us rederive this result. Consider the Markov process generated by the Metropolis algorithm: $\Delta \phi$ is accepted if $e^{-\Delta \mathcal{H}} - 1$ is positive; otherwise, it is accepted only with probability $e^{-\Delta \mathcal{H}}$. Employing the step function $\theta(x)$, the update rules for each lattice site can be written as

$$\phi_a(t + \delta t, x) = \phi_a(t, x) + \theta(e^{-\Delta \mathcal{H}} - 1) \Delta \phi_a$$
$$+ \theta(1 - e^{-\Delta \mathcal{H}}) e^{-\Delta \mathcal{H}} \Delta \phi_a, \qquad (A43a)$$

$$= \phi_a(t, x) + \Delta \phi_a$$
$$+ \theta(1 - e^{-\Delta \mathcal{H}})(e^{-\Delta \mathcal{H}} - 1) \Delta \phi_a. \qquad (A43b)$$

In the limit of small δt, $\Delta \phi_a$ is small, and we can Taylor expand the energy and the probability, obtaining

$$\phi_a(t + \delta t, x) = \phi_a(t, x) + \Delta\phi_a$$
$$+ \theta\left(\frac{\delta\mathcal{H}}{\delta\phi}\sqrt{2\delta t\Gamma_0}\xi_0\right)\left(-\frac{\delta\mathcal{H}}{\delta\phi}\right)2\delta t\Gamma_0\xi_0^2.$$
$$\text{(A44)}$$

Taking averages and noting that the θ function vanishes for half of the realizations, one immediately reproduces Eqs. (A42a) and (A42b).

To iterate over the sites, we loop over the lattice in a checkerboard pattern, first updating all of the even sites, and then updating the odd sites. Since the interactions are nearest neighbors only, the even site updates are independent of each other and can be done in any order. In addition, the checkerboard Metropolis updates maintain the lattice translational invariance and are easy to implement with PETSC and MPI [36,37].

Finally we turn to the step size δt. We would like the computer time required to thermalize modes of wavelength $\sim a$ to be as short as possible. If δt is small, then the steps are always accepted, but lead only to a small change in ϕ; equilibration then requires many steps. If δt is large, then $\Delta\phi$ is large, but the updates are always rejected, again requiring many steps. We have found that choosing $\delta t = 0.04/\Gamma_0$ leads to an accept-reject probability of approximately 0.5, optimizing these considerations.

c. Viscous steps for charges n_A and n_V

We are considering the evolution equation $\partial_t U = O_C(U)$. Since each charge in the tensor n_{ab} is independent we will dispense with the flavor indices in the rest of this section. All the updates described here will be applied in sequence to the three axial charges n_A^s and the three vector charges n_V^s. The continuum equation to be solved is the stochastic diffusion equation

$$\partial_t n + \partial_i j^i = 0, \qquad j^i = -\frac{\sigma_0}{\chi}\partial^i n + \Xi^i, \qquad \text{(A45)}$$

and equilibrium effective Hamiltonian is[6]

$$H = \int d^3x \frac{n^2}{2\chi_0}. \qquad \text{(A47)}$$

To generate the Langevin dynamics in (A45) we will again use Metropolis steps. In order to get the correct diffusive dynamics at long wavelengths the charge must be

---

[6]Again this action describes only one isospin component of the isoaxial or isovector charge. In general

$$\mathcal{H} = \int d^3x\left(\frac{\vec{n}_A \cdot \vec{n}_A}{2\chi_0} + \frac{\vec{n}_V \cdot \vec{n}_V}{2\chi_0}\right) = \frac{1}{4\chi_0}\int d^3x n_{ab}n_{ab}, \quad \text{(A46)}$$

and $n_{ab}n_{ab}$ is written n^2 in the majority of the text.

exactly conserved by the update proposals. We therefore update the cells in pairs by making a Metropolis proposal for the charge transferred between two cells over a time δt.

The figure below shows a few sites of the lattice, with the even sites painted gray. Integrating (A45) over the spatial volume of lattice cell A and time δt, the discretized equation of motion for the charge takes the form

$$\hat{n}(\hat{t} + \delta\hat{t}, \hat{x}) = \hat{n}(\hat{t}, \hat{x}) - (Q_+^x - Q_-^x) - (Q_+^y - Q_-^y)$$
$$- (Q_+^z - Q_-^z), \qquad \text{(A48)}$$

where, for example, Q_+^x is the charge transfer between A and B over a time δt. (For clarity below we have restored the hats to indicate quantities in lattice units, e.g., $\hat{n} = na^3$):
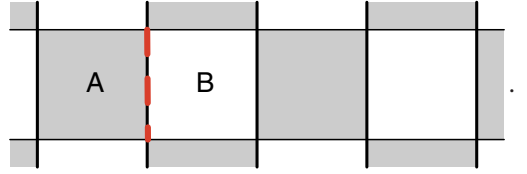
The proposed Metropolis flux through the interface is

$$Q_+^x = q = \sqrt{2\hat{\sigma}_0\delta\hat{t}}\xi_0, \qquad \text{(A49)}$$

where again ξ_0 is a uniform random number with unit variance. Thus the proposed update for cells A and B is

$$\hat{n}_A \to \hat{n}_A - q, \qquad \text{(A50)}$$

$$\hat{n}_B \to \hat{n}_B + q, \qquad \text{(A51)}$$

and change in action by the proposed change is

$$\Delta\hat{\mathcal{H}} = \frac{(\hat{n}_B + q)^2}{2\hat{\chi}_0} + \frac{(\hat{n}_A - q)^2}{2\hat{\chi}_0} - \frac{\hat{n}_B^2}{2\hat{\chi}_0} - \frac{\hat{n}_A^2}{2\hat{\chi}_0}, \qquad \text{(A52)}$$

$$= (\hat{n}_B - \hat{n}_A)\frac{q}{\hat{\chi}_0} + O(q^2). \qquad \text{(A53)}$$

The proposed updated is accepted with probability $\min(1, \exp(-\Delta\hat{\mathcal{H}}))$. Then it is easy to see that mean charge transfer is

$$\bar{q} = -(\hat{n}_B - \hat{n}_A)\frac{\hat{\sigma}_0}{\hat{\chi}_0}\delta\hat{t}, \qquad \text{(A54)}$$

$$\simeq -a^2\delta t D_0\partial_x n, \qquad \text{(A55)}$$

which is the expected charge transfer for a diffusive step. Finally, is easy to show that the flux $\Xi^x \simeq q/(\delta t a^2)$ has the expected variance. Thus for small δt the Markov updates produce an equivalent update to the Langevin step.

To iterate over the faces of the lattice we again divide the cells into a checkerboard pattern. We first do the Metropolis updates for all of the x_+ interfaces for all of the even cells, i.e., cell A is even and cell B is odd as shown in the figure above. These updates are independent of each other and can be done in any order. This step is followed by Metropolis updates of the x_- interfaces of the even cells, i.e., now cell A is odd and cell B is even. Then we proceed to update the y and z directions in a similar manner. To eliminate potential bias, the order of the (x, y, z) iterations and the $(+, -)$ iterations are each randomly shuffled for each iteration of the C stage of the Markov chain.

d. Real-time correlation functions

In this section we describe how the correlations functions and their Fourier transforms are computed. The correlation functions $G(t)$ for $t > 0$ are computed with

$$G(t) = \frac{1}{t_2 - t_1} \sum_{t'=t_1}^{t_2} \Delta t_p O(t') O(t' + t), \quad \text{(A56)}$$

and the error is estimated with simple blocking with 5–10 blocks. Here $\Delta t_p = p \Delta t$ where p is the accept reject probability as discussed in Appendix A 2 a. Taking $z = 0.7 z_{pc}$ with $H = 0.003$ to give representative numbers (see Fig. 5), we note that the correlation time of the system is ~ 400, while the total evolution time of the simulations is $t_2 - t_1 \sim 10^6$. $G(t)$ is recorded with t up to $t_{\max} \sim 4000$. We have discarded the first $t_1 \sim 10000$ simulation steps, ensuring proper thermalization, and checked that $G(t)$ is insensitive to t_1 and t_2. Since $G(-t) = G(t)$, the Fourier transform $G(\omega)$ is computed by

$$G(\omega) = 2 \sum_{t=0}^{t_{\max}} \Delta t_p G(t) \cos(\omega t) e^{-t/\Lambda}, \quad \text{(A57)}$$

where $\Lambda \sim 1200$ is a cutoff limiting the contributions of the late-time noise to the integral. The results were insensitive to the form of the cutoff and Λ. For different runs the correlation times can be somewhat longer and Λ and $t_{\max}$ are increased accordingly.

APPENDIX B: THERMODYNAMICS AND STATICS OF THE MODEL

1. Fixing the critical temperature

In this appendix we will describe our (conventional) strategy for locating the critical point of the model, by adjusting the bare coupling m_0^2. A good summary of the technique is given in [38]. Throughout this section we set $\lambda = 4$ (somewhat arbitrarily) and $H = 0$. After a preliminary search in m_0^2, we ran a set of long simulations at $m_0^2 = -4.812$ for $N = 16, 24, 32, 48, 64$. For each of these simulations, we used reweighted samples to compute the

Binder cumulant [43] for a range of m_0^2. More explicitly we computed

$$\langle M^2 \rangle = \frac{\sum_t e^{-\frac{1}{2}\delta m_0^2 \sum_x \phi^2(t,x)} M_a(t) \cdot M_a(t)}{\sum_t e^{-\frac{1}{2}\delta m_0^2 \sum_x \phi^2(t,x)}}, \quad \text{(B1)}$$

$$\langle (M^2)^2 \rangle = \frac{\sum_t e^{-\frac{1}{2}\delta m_0^2 \sum_x \phi^2(t,x)} (M_a(t) \cdot M_a(t))^2}{\sum_t e^{-\frac{1}{2}\delta m_0^2 \sum_x \phi^2(t,x)}}, \quad \text{(B2)}$$

and then determine the Binder cumulant:

$$U_4 \equiv \frac{\langle (M^2)^2 \rangle}{\langle M^2 \rangle^2}. \quad \text{(B3)}$$

A plot of U_4 for our $N = 16, 32, 64$ samples is shown in the left panel of Fig. 12.

In the high-temperature phase, the fluctuations of the order parameter are Gaussian and the Binder cumulant reaches $(N + 2)/N = 1.5$, while in the low-temperature phase the system is ordered and the Binder cumulant is unity. In the critical region (where the system size is of order of the correlation length) the Binder cumulant transitions between 1 and 1.5, and approaches a universal value U_4^c at the critical temperature for large L [44]. From a precision study by Hasenbusch [39], we have taken this asymptotic value to be $U_4^c = 1.0945(1)$. Now, for each L, we determined a value of m_0^2, denoted $m_\times^2(L)$, where the Binder cumulant reaches U_4^c (see figure). For large L the expected scaling of $m_\times^2(L) - m_c^2$ is

$$m_\times^2(L) - m_c^2 = \frac{C_1}{L^{1/\nu+\omega}}, \quad \text{(B4)}$$

and this scaling can be used to determine m_c^2. Then we fit $m_\times^2(L)$ with the functional form in (B4) to find the value of m_c^2 quoted in the body of the text in (30). A plot of our fit is shown in the right panel of Fig. 12 and has $\chi^2/\text{dof} = 0.5$, suggesting that the error bars have been slightly overestimated.

2. Thermodynamics on the critical line

In this section we continue the discussion in Sec. III A, and determine the nonuniversal parameter H_0 by making a scan on the critical line.

In practice, we made a scan only approximately on the critical line at $m^2 = -4.8130$, and then used reweighting to determine $\bar{\sigma}$ at our nominal value of $m_c^2 = -4.8110$. In the scaling theory the condensate takes the form

$$\bar{\sigma} = h^{1/\delta}(f_G(z, z_L) + h^{\omega \nu_c} f_G^{(1)}(z, z_L)), \quad \text{(B5)}$$

where in addition to the scaling variables h and z, we have included an additional dependence on the system size L
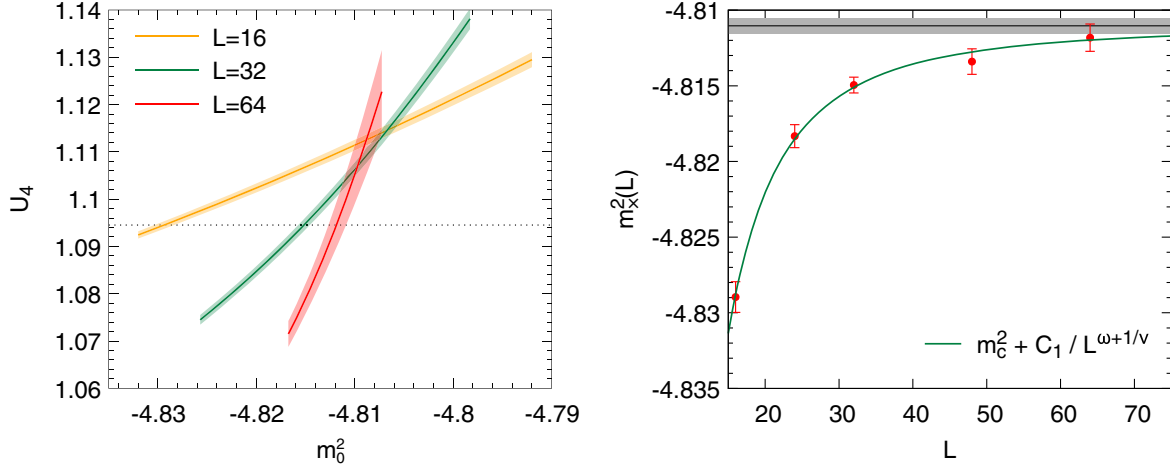
FIG. 12. (Left) The Binder cumulant U_4 as a function of m_0^2 and L. For clarity, the $L = 24$ and $L = 48$ results are not shown. The asymptotic value of the Binder cumulant U_4^c is shown as the dotted line, and is taken from [39]. The crossing points, $m_\times^2(L)$, are when bands cross the dotted line. (Right) A fit to the Binder crossing formula in (B4) which determines the critical parameter $m_c^2 = -4.8110(4)$.

through the scaling variable $z_L = L_0/Lh^{\nu_c}$, and its associated constant L_0 [6]. The scaling function $f_G(z, z_L)$ has been parametrized for $z_L = [0, 1.2]$ by Engels and Karsch [6] (see their Eq. 29). We have also included a subleading scaling function, $f_G^{(1)}(z, z_L)$, which provides a correction to the leading asymptotics close to T_c. We are working on the critical line where $z = 0$, and the dependence on z_L is weak for L large. Thus we will neglect the dependence on z_L in the subleading term and describe our data with the form

$$\bar{\sigma} = h^{1/\delta}(f_G(0, z_L) + h^{\omega\nu_c}C_H). \tag{B6}$$

For the critical exponents here and below we use the results from [6]:

$$\beta = 0.380(2), \qquad \delta = 0.4824(9), \tag{B7}$$

and then used the hyperscaling relations to determine all others, e.g., $d\nu = \beta(1 + \delta) \simeq 2.213$. We have taken $\omega = 0.77$ for the subleading exponent from [39]. The data for $\bar{\sigma}$ on 32^3 and 64^3 lattices on the critical line are shown in the left panel of Fig. 1 in the body of the text. They were fit in the range $z_L = [0, 1.2]$ with (B6), which fixes the three fit parameters for H_0, L_0, and C_H:

$$H_0 = 5.15(15), \quad L_0 = 0.97(4), \text{ and } C_H = 0.54(4), \tag{B8}$$

with $\chi^2/\text{dof} = 2$. H_0 is recorded in Eq. (30). Also shown in the left panel of Fig. 1 is the predicted magnetization from the fit at infinite volume (the dashed line). We see that already at $L = 64$, we are essentially at infinite volume for the range of H considered in this work. Indeed a simple two-parameter fit to our $L = 64$ results (not shown) with a

simple form, $\bar{\sigma} = (H/H_0)^{1/\delta}(1 + C_H(H/H_0)^{\omega\nu_c})$, yields compatible results for H_0.

3. Thermodynamics at $H = 0$

In this section we continue the discussion in Sec. III A, and determine the nonuniversal parameter $\mathfrak{m}^2$ (or the amplitude B) by making a scan at $H = 0$. By measuring $\langle M^2\rangle$ we will extract the condensate, Σ, at infinite volume and zero field defined in (31).

The leading deviation of $\langle M^2\rangle$ from Σ^2 at finite volume comes from the fluctuations of long-wavelength Goldstone modes, and can be neatly analyzed with a Euclidean pion effective theory [40], which was briefly discussed in Appendix B 4. The resulting expansion relating $\langle M^2\rangle$ and Σ^2 is only for $f^2(T)L \gg 1$, and takes the form

$$\langle M^2\rangle = \Sigma^2\left(\rho_1^2 + \frac{8\rho_2}{f^4L^2}\right) + O((f^2L)^{-3}). \tag{B9}$$

Here the symmetry group $O(N)$ is broken to $O(N-1)$, ρ_1 and ρ_2 are expansions in $1/L$:

$$\rho_1 = 1 + \frac{(N-1)\beta_1}{2f^2L} - \frac{(N-1)(N-3)}{8f^4L^2}(\beta_1^2 - 2\beta_2), \tag{B10}$$

$$\rho_2 = \frac{(N-1)\beta_2}{4}, \tag{B11}$$

with the shape coefficients that record specific sums over the discretized Fourier modes of a cubic box of length L:

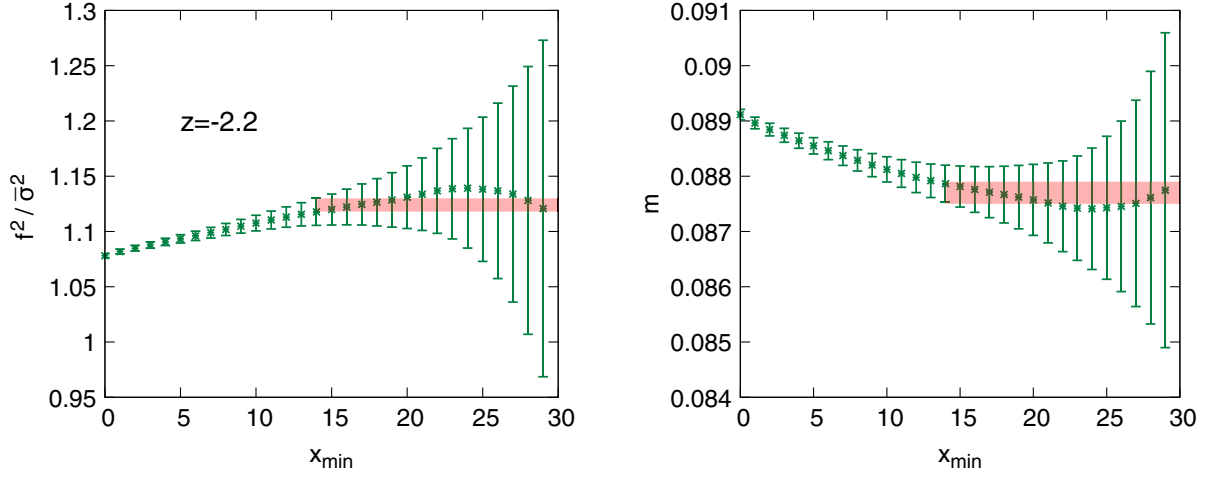$$\beta_1 = 0.225785, \qquad \beta_2 = 0.010608. \tag{B12}$$

FIG. 13.   Pion decay constant and static screening mass extracted from a single-state fit of the pion wall-to-wall static correlator $D(x)$. To remove the contamination from higher states, we restrict our fit (not shown) to the range $[x_{\min}, N - x_{\min} - 1]$. We plot here the fitted parameters as a function of $x_{\min}$. Our nominal values are shown in green and computed by averaging the results for $x_{\min} > 15$ once the values have plateaued.

Substituting the shape coefficients, setting $N = 4$, and finally expanding in $1/L$ yields the expansion we will use:

$$\langle M^2 \rangle = \Sigma^2 \left[1 + \frac{0.677355}{f^2 L} + \frac{0.156028}{f^4 L^2} + O((f^2 L)^{-3}) \right].$$

(B13)

To extract $\Sigma(T)$ we performed a sequence of simulations at $L = 16, 24, 32, 48, 64$ at $H = 0$. We then used (B9) with $N = 4$ to fit $f^2(T)$ and $\Sigma(T)$ using the $L = 32, 48$, and 64 points (not shown). The difference in the first and second orders in the expansion was used to estimate the systematic uncertainty in the extracted values of f^2 and Σ. For $\Sigma(T)$ this is smaller than our statistical uncertainty, which would not have been the case if only the leading term $1/L$ term in the expansion (B13) had been used. We also found that the quadratic term provides a better description of the data with no additional parameters, providing credence to the pion EFT in this range of temperatures and volumes.

4. Extracting the pion's decay constant and screening mass

The aim of this section is to verify the static part of the GOR formula:

$$f^2 m^2 = H\bar{\sigma},$$

(B14)

which is discussed in Sec. III B. To this end, we return to our simulation in the broken phase and perform some more static measurements. The magnetization is straightforward to measure

$$\bar{\sigma} = 0.34906 \pm 0.00003(\text{stat.}),$$

(B15)

and gives for the right-hand side

$$H\bar{\sigma} = (1.04718 \pm 0.00009(\text{stat.})) \times 10^{-3}.$$

(B16)

To measure the pion decay constant f^2 and the screening mass m, we follow [41] and fit (not shown) the static pion wall-to-wall static correlator:

$$D(x) \equiv \frac{1}{3L^2} \sum_s \sum_{y,y',z,z'} \langle \pi_s(t=0,x,y,z) \pi_s(t=0,x=0,y',z') \rangle$$

(B17)

to a single-state ansatz in a periodic box of size L:

$$D(x) = \frac{\bar{\sigma}^2}{2mf^2} \frac{e^{-mx} + e^{-m(L-x)}}{1 - e^{-mL}}.$$

(B18)

To reduce the remaining effects of higher states, we reduce the range of our fit to $[x_{\min}, L - x_{\min} - 1]$ and study the dependence of the parameters on $x_{\min}$. Their nominal value is then extracted by fitting the resulting plateaus. This procedure is illustrated in Fig. 13 and leads to the following determination:

$$\frac{f^2}{\bar{\sigma}^2} = 1.124 \pm 0.006(\text{stat.}),$$

(B19)

$$m = (8.77 \pm 0.02(\text{stat.})) \times 10^{-2},$$

(B20)

leading to

$$f^2 m^2 = (1.053 \pm 0.007(\text{stat.})) \times 10^{-3}.$$

(B21)

We see that the static GOR relation is satisfied within statistical errors, as displayed in (39) in the body of the text.

[1] Robert D. Pisarski and Frank Wilczek, Remarks on the chiral phase transition in chromodynamics, Phys. Rev. D **29,** 338 (1984).

[2] Krishna Rajagopal and Frank Wilczek, Static and dynamic critical phenomena at a second order QCD phase transition, Nucl. Phys. **B399,** 395 (1993).

[3] Doug Toussaint, Scaling functions for o(4) in three dimensions, Phys. Rev. D **55,** 362 (1997).

[4] K. Kanaya and S. Kaya, Critical exponents of a three dimensional O(4) spin model, Phys. Rev. D **51,** 2404 (1995).

[5] J. Engels and F. Karsch, The scaling functions of the free energy density and its derivatives for the 3D O(4) model, Phys. Rev. D **85,** 094506 (2012).

[6] J. Engels and F. Karsch, Finite size dependence of scaling functions of the three-dimensional O(4) model in an external field, Phys. Rev. D **90,** 014501 (2014).

[7] Francesco Parisen Toldin, Andrea Pelissetto, and Ettore Vicari, The 3-D O(4) universality class and the phase transition in two flavor QCD, J. High Energy Phys. 07 (2003) 029.

[8] Agostino Butti, Andrea Pelissetto, and Ettore Vicari, On the nature of the finite temperature transition in QCD, J. High Energy Phys. 08 (2003) 029.

[9] Jens Braun and Bertram Klein, Finite-size scaling behavior in the O(4)-Model, Eur. Phys. J. C **63,** 443 (2009).

[10] Jens Braun, Bertram Klein, and Piotr Piasecki, On the scaling behavior of the chiral phase transition in QCD in finite and infinite volume, Eur. Phys. J. C **71,** 1576 (2011).

[11] Jens Braun, Bertram Klein, and Bernd-Jochen Schaefer, On the phase structure of QCD in a finite volume, Phys. Lett. B **713,** 216 (2012).

[12] Jens Braun, Wei-jie Fu, Jan M. Pawlowski, Fabian Rennecke, Daniel Rosenblüh, and Shi Yin, Chiral susceptibility in (2 + 1)-flavour QCD, Phys. Rev. D **102,** 056010 (2020).

[13] H. T. Ding, P. Hegde, O. Kaczmarek, F. Karsch, A. Lahiri, S.-T. Li, S. Mukherjee, H. Ohno, P. Petreczky, C. Schmidt, and P. Steinbrecher, Chiral Phase Transition Temperature in (2 + 1)-Flavor QCD, Phys. Rev. Lett. **123,** 062002 (2019).

[14] Olaf Kaczmarek, Frithjof Karsch, Anirban Lahiri, Lukas Mazur, and Christian Schmidt, QCD phase transition in the chiral limit, arXiv:2003.07920.

[15] Ulrich Heinz and Raimond Snellings, Collective flow and viscosity in relativistic heavy-ion collisions, Annu. Rev. Nucl. Part. Sci. **63,** 123 (2013).

[16] D. T. Son, Hydrodynamics of Nuclear Matter in the Chiral Limit, Phys. Rev. Lett. **84,** 3771 (2000).

[17] Eduardo Grossi, Alexander Soloviev, Derek Teaney, and Fanglida Yan, Transport and hydrodynamics in the chiral limit, Phys. Rev. D **102,** 014042 (2020).

[18] Eduardo Grossi, Alexander Soloviev, Derek Teaney, and Fanglida Yan, Soft pions and transport near the chiral critical point, Phys. Rev. D **104,** 034025 (2021).

[19] D. Devetak, A. Dubla, S. Floerchinger, E. Grossi, S. Masciocchi, A. Mazeliauskas, and I. Selyuzhenkov, Global fluid fits to identified particle transverse momentum spectra from heavy-ion collisions at the Large Hadron Collider, J. High Energy Phys. 06 (**2020**) 044.

[20] Anthony Guillen and Jean-Yves Ollitrault, Fluid velocity from transverse momentum spectra, Phys. Rev. C **103,** 064911 (2021).

[21] Govert Nijs, Wilke van der Schee, Umut Gürsoy, and Raimond Snellings, Bayesian analysis of heavy ion collisions with the heavy ion computational framework Trajectum, Phys. Rev. C **103,** 054909 (2021).

[22] Expression of Interest for an ALICE ITS Upgrade in LS3, http://cds.cern.ch/record/2644611 (2018).

[23] P. C. Hohenberg and B. I. Halperin, Theory of dynamic critical phenomena, Rev. Mod. Phys. **49,** 435 (1977).

[24] Jurgen Berges, Soren Schlichting, and Denes Sexty, Dynamic critical phenomena from spectral functions on the lattice, Nucl. Phys. **B832,** 228 (2010).

[25] Sören Schlichting, Dominik Smith, and Lorenz von Smekal, Spectral functions and critical dynamics of the $O(4)$ model from classical-statistical lattice simulations, Nucl. Phys. **B950,** 114868 (2020).

[26] Dominik Schweitzer, Sören Schlichting, and Lorenz von Smekal, Spectral functions and dynamic critical behavior of relativistic Z_2 theories, Nucl. Phys. **B960,** 115165 (2020).

[27] Dominik Schweitzer, Sören Schlichting, and Lorenz von Smekal, Critical dynamics of relativistic diffusion, arXiv:2110.01696.

[28] D. T. Son and M. A. Stephanov, Dynamic universality class of the QCD critical point, Phys. Rev. D **70,** 056001 (2004).

[29] D. T. Son and Misha A. Stephanov, Pion Propagation Near the QCD Chiral Phase Transition, Phys. Rev. Lett. **88,** 202302 (2002).

[30] D. T. Son and Misha A. Stephanov, Real time pion propagation in finite temperature QCD, Phys. Rev. D **66,** 076011 (2002).

[31] I. E. Dzyaloshinskii and G. E. Volovick, Poisson brackets in condensed matter physics, Ann. Phys. (N.Y.) **125,** 67 (1980).

[32] L. D. Landau and E. M. Lifshitz, *Statistical Physics, Part 1*, Course of Theoretical Physics Vol. 5 (Butterworth-Heinemann, Oxford, 1980).

[33] C. Kittel, *Elementary Statistical Physics*, Dover Books on Physics Series (Dover Publications, New York, 2004).

[34] Akira Onuki, *Phase Transition Dynamics* (Cambridge University Press, Cambridge, England, 2002), 10.1017/CBO9780511534874.

[35] Guy D. Moore, The sphaleron rate: Bodeker's leading log, Nucl. Phys. **B568,** 367 (2000).

[36] Satish Balay *et al.*, PETSc Web page, https://petsc.org/ (2021).

[37] Satish Balay, William D. Gropp, Lois Curfman McInnes, and Barry F. Smith, Efficient management of parallelism in object oriented numerical software libraries, in *Modern Software Tools in Scientific Computing*, edited by E. Arge, A. M. Bruaset, and H. P. Langtangen (Birkhäuser Press, 1997), pp. 163–202.

[38] Peter Brockway Arnold and Guy D. Moore, Monte Carlo simulation of O(2) ϕ^4 field theory in three-dimensions,

Phys. Rev. E **64**, 066113 (2001); Erratum, Phys. Rev. E **68**, 049902(E) (2003).

[39] Martin Hasenbusch, Eliminating leading corrections to scaling in the three-dimensional O(N) symmetric ϕ^4 model: $N = 3$ and $N = 4$, J. Phys. A **34**, 8221 (2001).

[40] P. Hasenfratz and H. Leutwyler, Goldstone boson related finite size effects in field theory and critical phenomena with O(N) symmetry, Nucl. Phys. **B343**, 241 (1990).

[41] J. Engels and O. Vogt, Longitudinal and transverse spectral functions in the three-dimensional O(4) model, Nucl. Phys. **B832**, 538 (2010).

[42] Robert D. Pisarski and Michel Tytgat, Propagation of cool pions, Phys. Rev. D **54**, R2989 (1996).

[43] *Monte Carlo Methods in Statistical Physics*, edited by K. Binder, Topics in Current Physics, Vol. 7 (Springer-Verlag, Berlin, Germany, 1986).

[44] Paul Springer and Bertram Klein, O(2)-scaling in finite and infinite volume, Eur. Phys. J. C **75**, 468 (2015).